

## Multichannel experimental and theoretical approach to the $^{12}\text{C}(^{18}\text{O}, ^{18}\text{F})^{12}\text{B}$ single-charge-exchange reaction at 275 MeV: Initial-state interaction and single-particle properties of nuclear wave functions

A. Spatafora <sup>1,2,\*</sup>, D. Carbone <sup>2</sup>, F. Cappuzzello <sup>1,2</sup>, M. Cavallaro <sup>2</sup>, L. Acosta,<sup>3</sup> C. Agodi,<sup>2</sup> P. Amador-Valenzuela <sup>4</sup>, T. Borello-Lewin,<sup>5</sup> G. A. Brischetto <sup>1,2</sup>, S. Calabrese,<sup>1,2</sup> D. Calvo,<sup>6</sup> V. Capirossi,<sup>6,7</sup> E. R. Chávez Lomelí <sup>3</sup>, I. Ciraldo <sup>1,2</sup>, G. De Gregorio <sup>8,9</sup>, F. Delaunay <sup>1,2,10</sup>, H. Djapo,<sup>11</sup> C. Eke <sup>12</sup>, P. Finocchiaro <sup>2</sup>, S. Firat,<sup>13</sup> M. Fisichella,<sup>2</sup> A. Foti,<sup>14</sup> A. Gargano <sup>8</sup>, A. Hacisalihoglu <sup>15</sup>, F. Iazzi <sup>6,7</sup>, L. La Faiuci,<sup>1,2</sup> R. Linares,<sup>16</sup> J. Lubian <sup>16</sup>, N. Medina <sup>17</sup>, M. Morales,<sup>17</sup> J. R. B. Oliveira <sup>5</sup>, A. Pakou <sup>18</sup>, L. Pandola <sup>2</sup>, H. Petrascu,<sup>19</sup> F. Pinna,<sup>6,7</sup> G. Russo,<sup>1,14</sup> O. Sgouros <sup>2</sup>, M. A. G. da Silveira,<sup>20</sup> S. O. Solakci,<sup>13</sup> V. Soukeras <sup>1,2</sup>, G. Souliotis,<sup>21</sup> D. Torresi <sup>2</sup>, S. Tudisco,<sup>2</sup> A. Yildirim,<sup>13</sup> and V. A. B. Zagatto<sup>5</sup>

(NUMEN Collaboration)

<sup>1</sup>*Dipartimento di Fisica e Astronomia “Ettore Majorana”, Università di Catania, Catania, Italy*

<sup>2</sup>*Istituto Nazionale di Fisica Nucleare, Laboratori Nazionali del Sud, Catania, Italy*

<sup>3</sup>*Instituto de Física, Universidad Nacional Autónoma de México, México City, México*

<sup>4</sup>*Instituto Nacional de Investigaciones Nucleares, Ocoyoacac, México*

<sup>5</sup>*Instituto de Física, Universidade de São Paulo, São Paulo, Brazil*

<sup>6</sup>*Istituto Nazionale di Fisica Nucleare, Sezione di Torino, Torino, Italy*

<sup>7</sup>*Dipartimento Scienza Applicata e Tecnologia, Politecnico di Torino, Torino, Italy*

<sup>8</sup>*Istituto Nazionale di Fisica Nucleare, Sezione di Napoli, Napoli, Italy*

<sup>9</sup>*Dipartimento di Matematica e Fisica, Università della Campania “Luigi Vanvitelli”, Caserta, Italy*

<sup>10</sup>*Laboratoire de Physique Corpusculaire de Caen, Normandie Université, ENSICAEN, UNICAEN, CNRS/IN2P3, Caen France*

<sup>11</sup>*Institute of Accelerator Technologies, Ankara University, Turkey*

<sup>12</sup>*Department of Mathematics and Science Education, Faculty of Education, Akdeniz University, 07058 Antalya, Turkey*

<sup>13</sup>*Department of Physics, Akdeniz University, 07058 Antalya, Turkey*

<sup>14</sup>*Istituto Nazionale di Fisica Nucleare, Sezione di Catania, Catania, Italy*

<sup>15</sup>*Institute of Natural Science, Karadeniz Teknik Üniversitesi, Trabzon, Turkey*

<sup>16</sup>*Instituto de Física, Universidade Federal Fluminense, Niteroi, Brazil*

<sup>17</sup>*Instituto de Pesquisas Energeticas e Nucleares IPEN/CNEN, São Paulo, Brazil*

<sup>18</sup>*Department of Physics, University of Ioannina and Hellenic Institute of Nuclear Physics, Ioannina, Greece*

<sup>19</sup>*Institutul National de Cercetare-Dezvoltare pentru Fizica si Inginerie Nucleara Horia Hulubei, Bucharest, Romania*

<sup>20</sup>*Centro Universitario FEI, Sao Bernardo do Campo, Brazil*

<sup>21</sup>*Department of Chemistry, University of Athens and Hellenic Institute of Nuclear Physics, Athens, Greece*



(Received 18 July 2022; accepted 23 January 2023; published 13 February 2023)

**Background:** Single-charge-exchange reactions are appropriate tools to study the nuclear response to one-particle/one-hole isospin probes, gaining additional interest from the connection to beta decay. This analogy has been recently extended to second order, connecting double-charge-exchange reactions and double beta decays. Nowadays, the availability of powerful experimental setups and advanced nuclear theories and models allows one to access precious information on key nuclear structure aspects embedded in the widely sought neutrinoless double beta decay.

**Purpose:** We intend to bring to light the main nuclear structure and reaction features involved in the  $^{18}\text{O} + ^{12}\text{C}$  collision at 275 MeV incident energy. In this paper, the main focus is on the role of the initial- and final-state interactions in the overall reaction dynamics and on the single-particle nuclear structure properties accessed via the study of single-nucleon transfer reactions. Forthcoming articles will be devoted to go into the details of the response to one- and two-particle/hole isospin probes.

**Methods:** Cross-section energy spectra and angular distributions were measured in a unique experimental setup for the  $^{12}\text{C}(^{18}\text{O}, ^{18}\text{O})^{12}\text{C}$  elastic and inelastic scattering, the  $^{12}\text{C}(^{18}\text{O}, ^{17}\text{O})^{13}\text{C}$  one-neutron stripping, the  $^{12}\text{C}(^{18}\text{O}, ^{19}\text{F})^{11}\text{B}$  one-proton pickup, and the  $^{12}\text{C}(^{18}\text{O}, ^{18}\text{F})^{12}\text{B}$  single-charge-exchange nuclear reactions. A unique comprehensive and coherent theoretical calculation, able to describe the whole network of direct reactions using state-of-the-art nuclear structure and reaction theories, was performed, and it is presented for the first time in this article. This *holistic* approach, applied both to the experimental and theoretical analysis, is the main feature and worth of the work here presented.

\* alessandro.spatafora@lns.infn.it

**Results:** The energy and angular resolutions achieved in each reaction channel allowed us to isolate specific transitions and to map the diffraction patterns in the angular distributions. The cross-section calculations describe well the experimental data, both in terms of the absolute values and diffraction patterns. Although the distorted wave Born approximation (DWBA) calculations prove to be accurate in describing all the studied channels, better results are achieved when the couplings to inelastic transitions in both the incoming and outgoing partitions are introduced, as done in the coupled channels Born approximation (CCBA) calculations. Otherwise, no real improvement is found when the coupling effects among different partitions are explicitly taken into account in the coupled reaction channels (CRC) calculations.

**Conclusions:** The multichannel approach proposed in this paper is a promising method for accurate investigations of direct reactions originating in heavy-ion collisions. This is quite appealing for the precise spectroscopy of heavy nuclei proposed in many areas of nuclear physics. An example is the NUMEN project with its challenging commitment to provide valuable information on neutrinoless double beta decay nuclear matrix elements from single- and double-charge-exchange cross-section measurements.

DOI: [10.1103/PhysRevC.107.024605](https://doi.org/10.1103/PhysRevC.107.024605)

## I. INTRODUCTION

Currently there is growing interest in direct nuclear reactions induced by heavy ions [1–3]. A characterizing feature of these processes is the pronounced localization of the reaction flux at the surface of the colliding systems. The complicated overlap of projectile and target nuclear densities results in an overall strong absorption of the incoming flux for central collisions, leaving the peripheral processes much less influenced by many-body aspects. The direct reactions occur as small perturbations of the outgoing elastic flux, connected to specific degrees of freedom [4,5].

In this context the availability of powerful experimental setups and advanced nuclear theories and models has allowed the extraction of accurate information on selected aspects of nuclear states. Studies of elastic and inelastic scattering are interesting to investigate nucleus-nucleus potential and nuclear deformation [6], respectively. One-nucleon transfer reactions give access to single-particle configurations in nuclear states [7,8]. Single-charge-exchange (SCE) reactions allow one to explore the nuclear response to one-particle/one-hole isospin probes [9,10]. Additional interest in SCE stems from the suggested connection to beta decay since in both processes the same initial and final nuclear states may be involved [10,11]. The exploration of this analogy was recently extended to second order, studying the connection between double-charge-exchange (DCE) reactions and double beta decays [1,12–15]. In this scenario, the rich spectroscopy accessible by direct reactions can provide precious information on key nuclear structure aspects embedded in the widely sought neutrinoless double beta decay ( $0\nu\beta\beta$ ).

A common feature in reported studies on heavy-ion induced direct reactions is that they are focused on few (often one) reaction channels at a time. In this way the information extracted from data analysis cannot be fully constrained and important parameters need to be taken either from other experimental studies performed in similar conditions, or by model calculations. Thus, a consistent approach to a broader ensemble of reaction channels explored under the same experimental conditions and consistently described by a unique theoretical framework is highly desirable.

Here we present for the first time a consistent study of  $^{12}\text{C}(^{18}\text{O}, ^{18}\text{O})^{12}\text{C}$  elastic and inelastic scattering,

$^{12}\text{C}(^{18}\text{O}, ^{17}\text{O})^{13}\text{C}$  and  $^{12}\text{C}(^{18}\text{O}, ^{19}\text{F})^{11}\text{B}$  one-nucleon transfer nuclear reactions at 275 MeV incident energy. Very seldom are such comprehensive studies found in the literature [16]. The choice of the projectile and target was driven by the available accurate information on the involved nuclear low-lying states in this mass region from both experimental results and large-scale shell-model studies, making this system an ideal benchmark for the proposed multichannel constrained technique.

Additional consistency in this study comes from the  $^{12}\text{C}(^{18}\text{O}, ^{16}\text{O})^{14}\text{C}$  two-neutron stripping reaction studied within the same experimental campaign and the same theoretical framework as in Ref. [17], where additional evidence of the giant pairing vibration in light nuclei is presented [3].

In the present article, data for the  $^{12}\text{C}(^{18}\text{O}, ^{18}\text{F})^{12}\text{B}$  single-charge-exchange reaction are shown for the first time. The analysis of the measured angular distributions for this channel requires the study of the competition between the direct meson exchange and the sequential transfer of two uncorrelated nucleons, both populating the same single-charge-exchange partition [11], whose results will be published in a forthcoming paper.

Here the focus is on the consistent approach to all the scrutinized channels of the present colliding system, with the aim to use then the same strategy for the exploration of isotopes of interest for  $0\nu\beta\beta$  decay.

The paper is organized as follows. Section II contains a brief description of the experimental setup, the measurement details, and the main observables extracted from the data reduction for the different reactions. Section III describes the theoretical approach adopted to calculate the cross sections, including both the reaction as well as the nuclear structure aspects. Based on the comparison between the measured and calculated cross sections, a discussion oriented toward the overall picture gained in such multichannel approach is presented in Sec. IV. Conclusions and perspectives are given in Sec. V.

## II. EXPERIMENTAL SETUP AND RESULTS

The experiment was performed at the Istituto Nazionale di Fisica Nucleare, Laboratori Nazionali del Sud (INFN-LNS)

TABLE I. Target thickness, range of scattering angles [ $\theta_{\text{lab}}^{\text{min}}$ ;  $\theta_{\text{lab}}^{\text{max}}$ ], central angle  $\theta_{\text{opt}}$ , and solid angle acceptance of the MAGNEX magnetic spectrometer for each explored reaction channel and experimental setup. Table from Ref. [18].

Channel		Target thickness ( $\mu\text{g}/\text{cm}^2$ )	[ $\theta_{\text{lab}}^{\text{min}}$ ; $\theta_{\text{lab}}^{\text{max}}$ ] (deg)	$\theta_{\text{opt}}$ (deg)	Solid angle (msr)
el. & inel. scattering	$^{12}\text{C}(^{18}\text{O}, ^{18}\text{O})^{12}\text{C}$	$60 \pm 3$	[3.5; 14.2]	7.5	49.2
		$400 \pm 20$		9.0	13.6
		$60 \pm 3$		13.5	49.2
$1n$ transfer	$^{12}\text{C}(^{18}\text{O}, ^{17}\text{O})^{13}\text{C}$	$200 \pm 10$	[3.1; 17.5]	8.0	13.6
		$60 \pm 3$		13.5	49.2
$1p$ transfer	$^{12}\text{C}(^{18}\text{O}, ^{19}\text{F})^{11}\text{B}$	$60 \pm 3$	[3.6; 16.1]	7.5	49.2
		$200 \pm 10$		8.0	13.6
		$60 \pm 3$		13.5	49.2
single-charge exchange	$^{12}\text{C}(^{18}\text{O}, ^{18}\text{F})^{12}\text{B}$	$60 \pm 3$	[3.2; 14.3]	7.5	49.2
		$200 \pm 10$		8.0	13.6
		$60 \pm 3$		13.5	49.2

in Catania. The  $^{18}\text{O}^{4+}$  ion beam was accelerated by the K800 Superconducting Cyclotron at 275 MeV bombarding energy. Thin foils of  $^{12}\text{C}$  were used as targets in the different experimental runs. The target thicknesses and other information on the experimental setup are listed in Table I for each of the analyzed reaction channels. The beam current at the target was measured by a Faraday cup (0.8 cm entrance diameter and 3 cm depth) located, along the beam direction, 15 cm downstream of the target. The Faraday cup was equipped with an electron suppressor polarized at  $-200$  V and a charge integrating circuit in order to access the total number of incident ions with a charge collection accuracy better than 10%.

The ejectiles, emerging from the beam-target interaction, were identified and analyzed in momentum by the MAGNEX magnetic spectrometer [19] and its focal plane detector [20,21]. The spectrometer optical axis was set at different angles  $\theta_{\text{opt}}$  for the different reactions, adopting in each case a specific configuration of the angular acceptance by setting movable horizontal and vertical slits located at the entrance of the spectrometer (see Table I).

The atomic and mass numbers and the charge state of the detected ions were extracted applying two different techniques. The atomic number is identified via the well known correlation between the measured energy loss  $\Delta E$  and residual energy  $E_{\text{resid}}$ . The mass number and charge state are determined by the correlation between  $E_{\text{resid}}$  and the position in the dispersive direction at the focal plane detector ( $x_{\text{foc}}$ ) [22–24]. In a recent paper by Calabrese *et al.* [25], it was shown that, in the case of similar experimental conditions, this approach ensures a strong rejection of background from misidentified ejectiles, allowing the measurement of cross sections lower than 1 nb.

The trajectory reconstruction technique, already described in previous works [26,27], was applied to access the momentum vector of the identified ejectiles at the target point.

The excitation energy  $E_x$  was calculated as the difference  $Q_0 - Q$ , where  $Q_0$  is the ground-state to ground-state  $Q$  value and  $Q$  is the  $Q$  value obtained by the missing mass technique based on relativistic kinematic transformations. Example excitation energy spectra for each of the analyzed

nuclear reactions are shown in Fig. 1. The energy resolution was slightly dependent on the reaction channel due to the different energy straggling produced by the ejectile/target interaction. In certain cases it was possible to single out transitions to specific states of the residual nuclei or at least to isolate transitions to groups of states, as described in the following sections. The absolute cross-section angular distributions were determined for many of such structures and isolated transitions.

#### A. $^{12}\text{C}(^{18}\text{O}, ^{18}\text{O})^{12}\text{C}$ elastic and inelastic scattering

The energy spectrum of the  $^{12}\text{C}(^{18}\text{O}, ^{18}\text{O})^{12}\text{C}$  elastic and inelastic scattering at angles between  $5^\circ$  and  $6^\circ$  in the laboratory reference frame is shown in Fig. 1(a). The energy resolution is  $\delta E_x \approx 0.6$  MeV in full width at half maximum (FWHM). This resolution, together with the low level density in the involved nuclei, made it possible to identify the observed peaks, which are listed in Table II.

TABLE II. Excitation energies ( $E_x$ ), total angular momentum and parity ( $J^\pi$ ) of the populated states and transferred orbital angular momenta ( $L$ ) in the  $^{12}\text{C}(^{18}\text{O}, ^{18}\text{O})^{12}\text{C}$  elastic and inelastic scattering at 275 MeV. Quality factors QF are calculated using Eq. (5) for each of the angular distributions shown in Figs. 2 and 3. The energies in the first column correspond to those listed in the legend of Fig. 1(a).

Peak label (MeV)	$E_x$ (MeV)		$L$	QF		
	$^{18}\text{O}$ ( $J^\pi$ ) [30]	$^{12}\text{C}$ ( $J^\pi$ ) [31]		DWBA	CCBA	CRC
0.00	0.000 ( $0^+$ )	0.000 ( $0^+$ )	0	0.63	0.76	0.74
1.98	1.982 ( $2^+$ )	0.000 ( $0^+$ )	2	0.49	0.64	0.65
3.60	3.554 ( $4^+$ )	0.000 ( $0^+$ )	4			
	3.633 ( $0^+$ )	0.000 ( $0^+$ )	0			
	3.920 ( $2^+$ )	0.000 ( $0^+$ )	2			
4.44	0.000 ( $0^+$ )	4.440 ( $2^+$ )	2	0.71	0.59	0.57
5.10	5.097 ( $3^+$ )	0.000 ( $0^+$ )	3	0.48	0.59	0.62
6.42	1.982 ( $2^+$ )	4.440 ( $2^+$ )	$2 \oplus 2$		0.72	0.73
7.65	0.000 ( $0^+$ )	7.654 ( $0^+$ )	0			
9.64	0.000 ( $0^+$ )	9.641 ( $3^+$ )	3	0.58	0.65	0.65

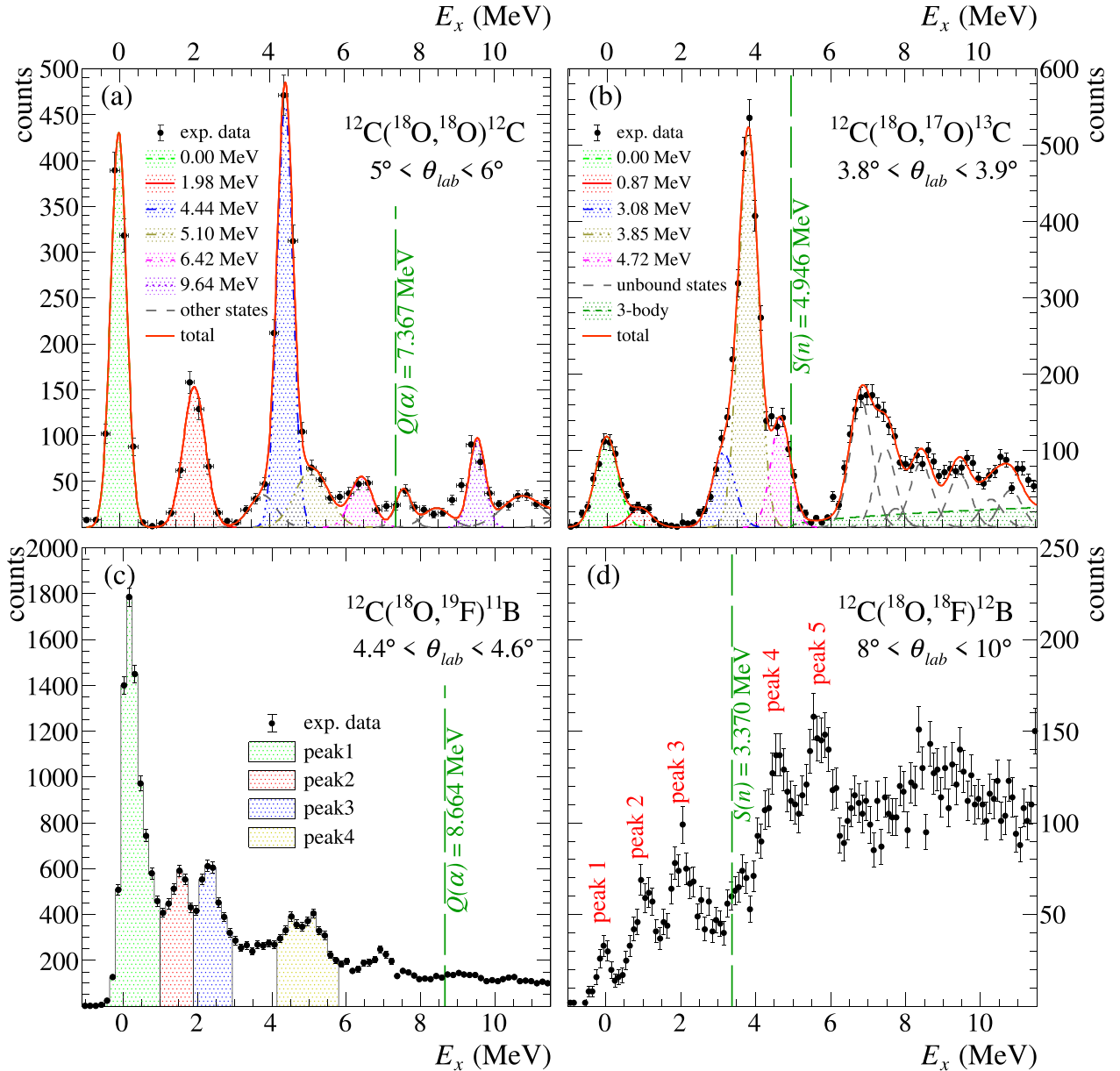


FIG. 1. Excitation energy spectra for the network of nuclear reactions involved in the multichannel study of the single-charge-exchange reactions coming from the  $^{18}\text{O} + ^{12}\text{C}$  collision at 275 MeV incident energy. (a)  $^{12}\text{C}(^{18}\text{O}, ^{18}\text{O})^{12}\text{C}$  elastic and inelastic scattering energy spectrum at  $5^\circ < \theta_{lab} < 6^\circ$ . Lines, obtained from best-fit procedure, identify peaks corresponding to the superposition of the projectile and target states, as labeled in the legend. (b)  $^{12}\text{C}(^{18}\text{O}, ^{17}\text{O})^{13}\text{C}$  one-neutron stripping energy spectrum at  $3.8^\circ < \theta_{lab} < 3.9^\circ$ . Lines, obtained from best-fit procedure, identify peaks corresponding to the superposition of the projectile and target states, as labeled in the legend. (c)  $^{12}\text{C}(^{18}\text{O}, ^{19}\text{F})^{11}\text{B}$  one-proton pickup energy spectrum at  $4.4^\circ < \theta_{lab} < 4.6^\circ$ . The hatched areas indicate the regions of interest for the study of the angular distributions as labeled in the legend. (d)  $^{12}\text{C}(^{18}\text{O}, ^{18}\text{F})^{12}\text{Be}$  single-charge-exchange energy spectrum at  $8^\circ < \theta_{lab} < 10^\circ$ .

The bound-state region of the spectrum is dominated by the transition to ground and to the collective  $2_1^+$  states at 1.982 and 4.440 MeV of projectile and target, respectively, whereas the fingerprint of their simultaneous excitation is visible in the structure at  $E_x \approx 6.42$  MeV.

The two-phonon triplet of the  $^{18}\text{O}$  ( $4_1^+$  at 3.555 MeV,  $0_2^+$  at 3.634 MeV, and  $2_2^+$  at 3.920 MeV) is not resolved in our spectra and corresponds to a structure centered at 3.6 MeV, very close to the strong peak at  $E_x \approx 4.44$  MeV. The two peaks

at  $E_x \approx 5.10$  MeV and  $E_x \approx 9.64$  MeV in Fig. 1(a) were attributed to the collective  $3_1^-$  states of  $^{18}\text{O}$  and  $^{12}\text{C}$ , respectively. The 7.654 MeV peak corresponding to the  $^{12}\text{C}$   $0_2^+$  Hoyle state was identified in the spectrum although the collected statistics was not enough to extract the angular distribution.

The excitation energy region of the  $^{12}\text{C}$  around 10 MeV has been extensively studied in recent years searching for the  $2_2^+$  state, considered the first excited state of the Hoyle rotational band, predicted by the  $\alpha$ -cluster model [28,29]. In

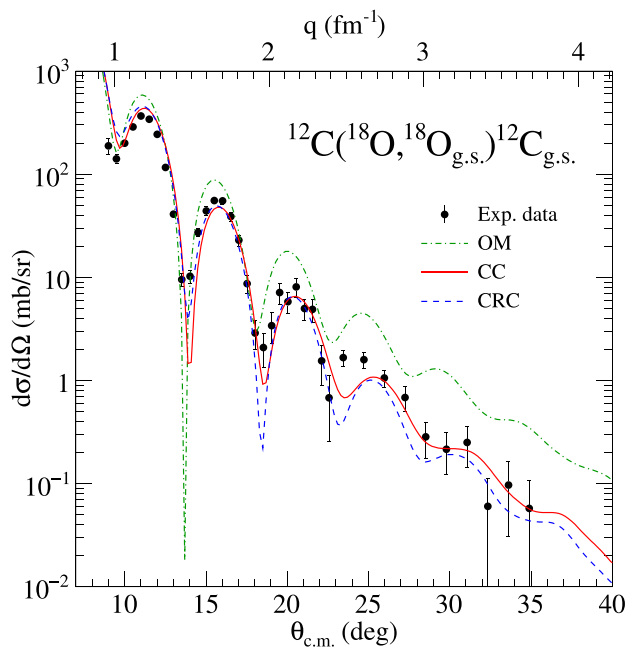


FIG. 2. Experimental cross-section angular distribution of the  $^{12}\text{C}(^{18}\text{O}, ^{18}\text{O})^{12}\text{C}$  elastic scattering at 275 MeV incident energy. Theoretical calculations for the elastic transition in OM, CC, and CRC approaches are shown with the green dashed, continuous red, and blue dot-dashed lines, respectively.

the study of Itoh *et al.* [29] a  $2^+$  state was observed at  $E_x = 9.84$  MeV with a FWHM of about 1 MeV, submerged by the broad  $0^+$  state at  $E_x = 9.93$  MeV and width of 2.7 MeV. Indeed, the peak at 9.64 MeV observed in our spectra could also contain contributions from these states. The comparison with the theoretical calculations will help in clarifying our interpretation of the peak as due to the population of the  $3_1^-$  state of  $^{12}\text{C}$ .

The multiple-fit procedure, shown in Fig. 1(a), was performed to extract the number of counts in the explored angular range, disentangling the contributions coming from the different transitions lying on the same excitation energy region. The width of each Gaussian function in the multiple-fit procedure was fixed according to the experimental energy resolution, including the recoil energy broadening due to the in-flight decay of the ejectile for the transitions in which it was found in a bound excited state.

The angular distributions of differential cross section were extracted for the ground-state, the 1.98 MeV, the 4.44 MeV, the 5.10 MeV, the 6.42 MeV, and the 9.64 MeV peaks. These angular distributions are shown in Figs. 2 and 3. The explored angular range was spanned in three independent measurements performed at different MAGNEX central angles, as listed in Table I. The three cross-section measurements were found to be in good agreement with each other without the need of any renormalization factor. The experimental points in Figs. 2 and 3 are obtained, in the overlap region between different angular sets, by a weighted average of the measured values. The error bars include uncertainties coming from the statistical contribution, solid angle estimation, and fitting

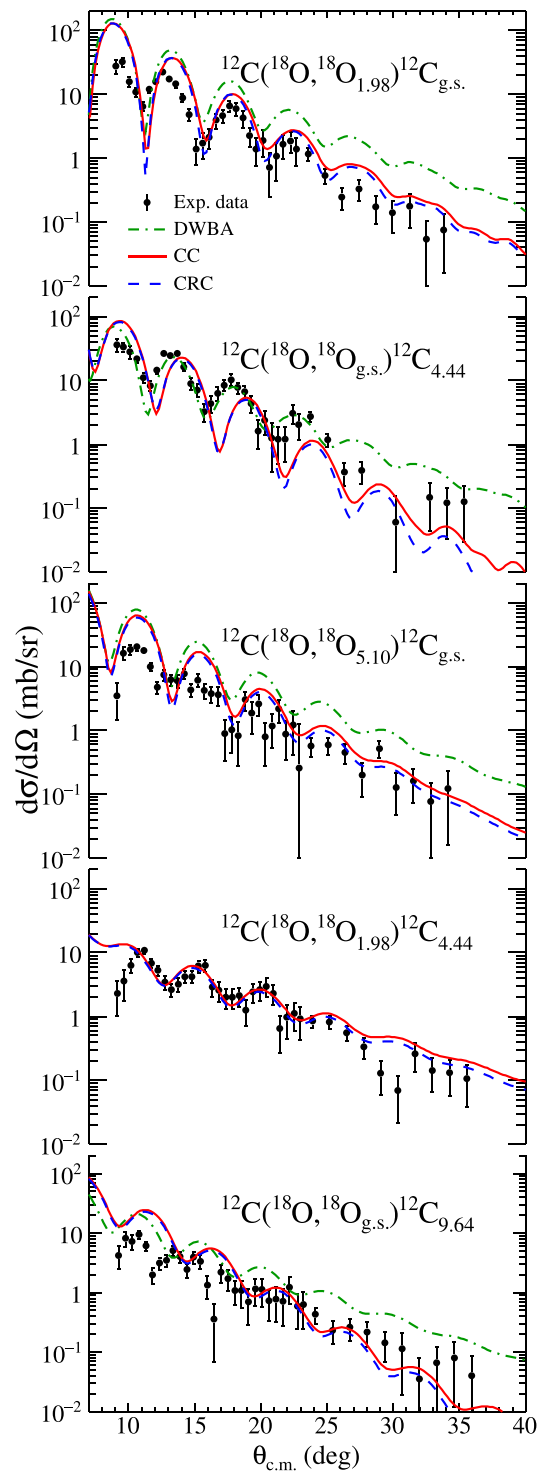


FIG. 3. Experimental cross-section angular distribution of the  $^{12}\text{C}(^{18}\text{O}, ^{18}\text{O})^{12}\text{C}$  inelastic scattering at 275 MeV incident energy associated with the peaks at 1.98, 4.44, 5.10, 6.42, and 9.64 MeV indicated in Fig. 1(a) and Table II. Theoretical calculations for the inelastic transitions in DWBA, CC, and CRC approaches are shown with the green dot-dashed, continuous red, and blue dashed lines, respectively.

procedure. An overall systematic uncertainty of about 10%, due to the determination of charge collection and target thickness, is common to all data points in the angular distributions

TABLE III. Excitation energies ( $E_x$ ), total angular momentum, and parity ( $J^\pi$ ) of the populated states and transferred orbital angular momenta ( $L$ ) in the  $^{12}\text{C}(^{18}\text{O}, ^{17}\text{O})^{13}\text{C}$  one-neutron stripping at 275 MeV. The theoretical cross sections  $\sigma_{\text{theo}}$  are integrated in the angular domain  $[0, 180^\circ]$ , and quality factors QF are calculated using Eq. (5) for each of the angular distributions shown in Fig. 4. The energies in the first column correspond to those listed in the legend of Fig. 1(b).

Peak label (MeV)	$E_x$ (MeV)		DWBA		CCBA		CRC	
	$^{17}\text{O}$ ( $J^\pi$ ) [35]	$^{13}\text{C}$ ( $J^\pi$ ) [36]	$\sigma_{\text{theo}}$ ( $\mu\text{b}$ )	QF	$\sigma_{\text{theo}}$ ( $\mu\text{b}$ )	QF	$\sigma_{\text{theo}}$ ( $\mu\text{b}$ )	QF
0.00	0.000 ( $5/2^+$ )	0.000 ( $1/2^-$ )	1787	0.64	1826	0.70	1702	0.68
0.87	0.871 ( $1/2^+$ )	0.000 ( $1/2^-$ )	629	0.71	653	0.72	606	0.71
3.08	3.055 ( $1/2^-$ )	0.000 ( $1/2^-$ )	896	0.73	928	0.70	892	0.67
3.85	0.000 ( $5/2^+$ )	3.089 ( $1/2^+$ )	573	0.82	404	0.74	392	0.79
	0.000 ( $5/2^+$ )	3.684 ( $3/2^-$ )	513		593		553	
4.64	0.000 ( $5/2^+$ )	3.854 ( $5/2^+$ )	11167	0.76	11447	0.78	10619	0.80
	0.871 ( $1/2^+$ )	3.089 ( $1/2^+$ )	239		194		192	
	0.871 ( $1/2^+$ )	3.684 ( $3/2^-$ )	199		225		213	
	0.871 ( $1/2^+$ )	3.854 ( $5/2^+$ )	4010		3368		3202	
6.88	3.055 ( $1/2^-$ )	3.684 ( $3/2^-$ )						
	0.000 ( $5/2^+$ )	6.864 ( $5/2^+$ )						
	3.055 ( $1/2^-$ )	3.854 ( $5/2^+$ )						
7.52	0.000 ( $5/2^+$ )	7.492 ( $7/2^+$ )						
	0.000 ( $5/2^+$ )	7.547 ( $5/2^-$ )						
7.71	0.000 ( $5/2^+$ )	7.686 ( $3/2^+$ )						
	0.871 ( $1/2^+$ )	6.864 ( $5/2^+$ )						
8.39	0.871 ( $1/2^+$ )	7.492 ( $7/2^+$ )						
	0.871 ( $1/2^+$ )	7.547 ( $5/2^-$ )						
9.50	0.000 ( $5/2^+$ )	9.500 ( $9/2^+$ )						
10.37	0.871 ( $1/2^+$ )	9.500 ( $9/2^+$ )						
10.80	0.000 ( $5/2^+$ )	10.753 ( $7/2^-$ )						
	0.000 ( $5/2^+$ )	10.819 ( $5/2^-$ )						
	0.000 ( $5/2^+$ )	10.996 ( $1/2^+$ )						

and it is not included in the error bars. The angular resolution is  $\delta\theta_{\text{c.m.}} \approx 0.5^\circ$  allowing a clear observation of the diffracting oscillation pattern in the angular distributions. The excitation energy and spin-parity of the states involved in the measured angular distribution, together with the transferred angular momentum  $L$ , are given in Table II.

### B. $^{12}\text{C}(^{18}\text{O}, ^{17}\text{O})^{13}\text{C}$ one-neutron stripping

The energy spectrum of the  $^{12}\text{C}(^{18}\text{O}, ^{17}\text{O})^{13}\text{C}$  one-neutron stripping reaction is shown in Fig. 1(b) for  $3.8^\circ < \theta_{\text{lab}} < 3.9^\circ$ . The obtained energy resolution is  $\delta E_x = 0.6$  MeV FWHM. The correspondence between the peaks observed in the spectrum and the states of projectile and target is indicated in Table III.

The spectrum of Fig. 1(b) resembles the one reported by Cavallaro *et al.* [32], measured at 84 MeV incident energy. In both spectra the strength is concentrated in the low excitation energy region ( $E_x < 5$  MeV). This is a result of the similar  $Q$ -value matching conditions [33] which give the optimal excitation energies  $E_x^{\text{opt}}(84 \text{ MeV}) = 1.6$  MeV and  $E_x^{\text{opt}}(275 \text{ MeV}) = -7.3$  MeV, and the favored transferred angular momenta  $L^{\text{opt}}(84 \text{ MeV}) = 1.5$  and  $L^{\text{opt}}(275 \text{ MeV}) = 1$ . As already noticed at 84 MeV [32], the transitions to well-known single-particle states of  $^{13}\text{C}$  products and  $^{17}\text{O}$  ejectiles are dominant. The same scenario was found in the study of the  $^{12}\text{C}(d, p)^{13}\text{C}$  reaction reported in Ref. [34], in which the weak population of states with more complex configurations

indicates that the direct transfer of one neutron is the leading mechanism.

A multiple-fit procedure, similar to that discussed for the spectrum of Fig. 1(a), was applied to the one-neutron stripping case. An example is shown in Fig. 1(b). A list of the different transitions lying underneath the same peak is detailed in Table III. The cross-section angular distributions were extracted for the peaks at  $E_x = 0.00, 0.87, 3.08, 3.85$ , and  $4.64$  MeV and are shown in Fig. 4. These correspond to the superposition of transitions to bound states of  $^{13}\text{C}$  (below the one-neutron separation energy  $S_n = 4.946$  MeV) and/or of  $^{17}\text{O}$  ( $S_n = 4.143$  MeV). Resembling the elastic scattering case, the explored angular range was covered by two independent measurements (see Table I) well matched without the need of any renormalization factor. The error bars include the same contributions as those for the elastic and inelastic scattering angular distributions.

### C. $^{12}\text{C}(^{18}\text{O}, ^{19}\text{F})^{11}\text{B}$ one-proton pickup

The excitation energy spectrum measured for the  $^{12}\text{C}(^{18}\text{O}, ^{19}\text{F})^{11}\text{B}$  one-proton pickup reaction at  $4.4^\circ < \theta_{\text{lab}} < 4.6^\circ$  is shown in Fig. 1(c). The energy resolution could not be easily extracted from the collected data due to the high level density in the  $^{19}\text{F}$  ejectile. To this extent, an energy resolution of  $\delta E_x \approx 0.6$  MeV was assumed, similarly to the other reaction channels.

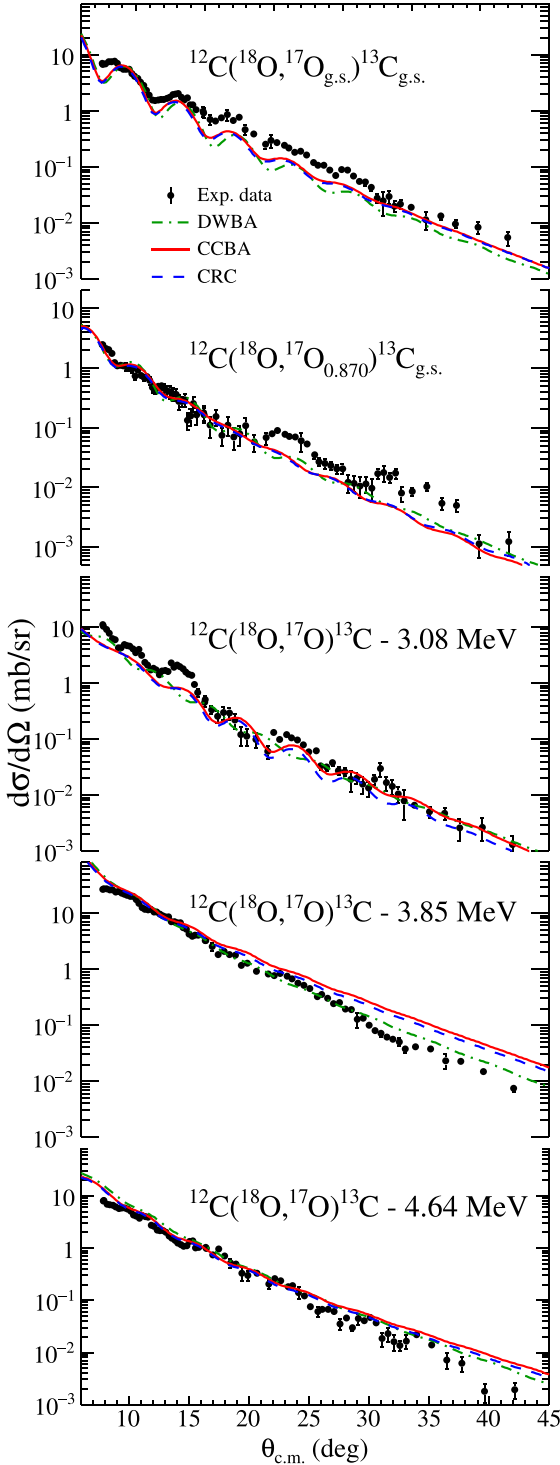


FIG. 4. Experimental cross-section angular distribution of the  $^{12}\text{C}(^{18}\text{O}, ^{17}\text{O})^{13}\text{C}$  one-neutron stripping at 275 MeV incident energy associated with the peaks at 0.00, 0.87, 3.08, 3.85, and 4.64 MeV indicated in Fig. 1(b) and Table III. Theoretical calculations of the one-neutron stripping nuclear reaction in DWBA, CCBA, and CRC approaches are shown with the green dot-dashed, continuous red, and blue dashed lines, respectively.

As already observed for the one-neutron stripping reaction, the strength is concentrated at energies below the alpha particle emission threshold at 8.664 MeV. This behavior is

compatible with the optimal matching conditions  $E_x^{\text{opt}} = -3.3$  MeV and  $L^{\text{opt}} = 2$  calculated according to Ref. [33]. We identified four main peaks [see Fig. 1(c)] described in terms of the  $^{19}\text{F}$  and  $^{11}\text{B}$  states as listed in Table IV.

The  $^{11}\text{B}$  ( $\frac{3}{2}^-$ ) ground state can be simply explained by the pick-up of one  $1p_{\frac{3}{2}}$  proton from the ground state (g.s.) of the  $^{12}\text{C}$ . The 2.124 ( $\frac{1}{2}^-$ ) and 5.020 ( $\frac{3}{2}^-$ ) MeV states can be described as the pickup of one proton from the  $1p_{\frac{1}{2}}$  and  $1p_{\frac{3}{2}}$  orbitals, respectively, starting from the  $^{12}\text{C}$  g.s. configuration in which two protons are found in the  $1p_{\frac{1}{2}}$  orbital. The states at 4.445 ( $\frac{5}{2}^-$ ) MeV and 6.76 ( $\frac{7}{2}^-$ ) MeV, visible in the spectrum of Fig. 5, attracted particular interest in the past [37,38]. Indeed, in order to be populated by the pickup of a proton from the  $^{12}\text{C}$  g.s., they should contain large admixtures of  $1f$  orbitals or a significant configuration of a  $1p_{\frac{3}{2}}$  proton hole coupled to the  $2^+$  core excitation of  $^{12}\text{C}$  at 4.440 MeV. This second hypothesis corresponds to two reaction paths: the excitation of the  $2^+$  state in the initial partition followed by the pickup of the  $1p_{\frac{3}{2}}$  proton or the pickup of a  $1p_{\frac{3}{2}}$  proton followed by the inelastic  $2^+$  excitation in the final partition. According to that, the proper treatment of such two-step processes requires the explicit inclusion of the couplings with the inelastic states in both the initial and final partitions, demanding sophisticated reaction calculations.

Similar arguments can be applied to the  $^{19}\text{F}$  level structure. The ground ( $\frac{1}{2}^+$ ), 0.197 ( $\frac{5}{2}^+$ ), and 1.554 ( $\frac{3}{2}^+$ ) MeV states are expected to have strong single-particle configurations with a proton in the  $2s_{\frac{1}{2}}$ ,  $1d_{\frac{3}{2}}$ , and  $1d_{\frac{5}{2}}$  orbitals, respectively. The 0.110 ( $\frac{1}{2}^-$ ) and 1.458 ( $\frac{3}{2}^-$ ) MeV negative-parity states can have single-hole components in the  $1p_{\frac{1}{2}}$  and  $1p_{\frac{3}{2}}$  shells. Regarding the 1.345 ( $\frac{5}{2}^-$ ) and 2.780 ( $\frac{9}{2}^+$ ) MeV states, we expect a very small contribution from single-particle configurations since they should involve the  $1f_{\frac{5}{2}}$  and  $1g_{\frac{9}{2}}$  orbitals that are far away from the Fermi level of  $^{18}\text{O}_{\text{g.s.}}$ . Thus, also for these states we expect important contributions from core excitation configurations involving the  $2^+$  [39,40] and  $3^-$  collective excitation of  $^{18}\text{O}$ .

In this case, we considered it unsafe to extract the counts using the multiple-fit technique described in the previous paragraphs. Instead, for each peak we just integrated the yield in the colored regions highlighted in Fig. 1(c). The obtained angular distributions are given in Fig. 5, in which the error bars include only the statistical and solid angle estimation uncertainties. The angular range was covered by three independent measurements performed at the central angles listed in Table I. Once again no renormalization factor was used for the cross sections.

#### D. $^{12}\text{C}(^{18}\text{O}, ^{18}\text{F})^{12}\text{B}$ single-charge exchange

An example of excitation energy spectrum for the  $^{12}\text{C}(^{18}\text{O}, ^{18}\text{F})^{12}\text{B}$  charge-exchange reaction measured in the angular region  $8^\circ < \theta_{\text{lab}} < 10^\circ$  is shown in Fig. 1(d).

Heavy-ion induced charge-exchange reactions populating odd-odd nuclei both in the projectile and target side typically produce energy spectra characterized by high level density

TABLE IV. Excitation energies ( $E_x$ ), total angular momentum and parity ( $J^\pi$ ) of the populated states and transferred orbital angular momenta ( $L$ ) in the  $^{12}\text{C}(^{18}\text{O}, ^{19}\text{F})^{11}\text{B}$  one-proton pickup at 275 MeV. The theoretical cross sections  $\sigma_{\text{theo}}$  are integrated in the angular domain  $[0, 180^\circ]$ , and quality factors  $QF$  are calculated using Eq. (5) for each of the angular distributions shown in Fig. 5. The labels in the first column correspond to those listed in the legend of Fig. 1(c).

Peak label	$E_x$ (MeV)		DWBA		CCBA		CRC	
	$^{19}\text{F}$ ( $J^\pi$ ) [30]	$^{11}\text{B}$ ( $J^\pi$ ) [41]	$\sigma_{\text{theo}}$ ( $\mu\text{b}$ )	QF	$\sigma_{\text{theo}}$ ( $\mu\text{b}$ )	QF	$\sigma_{\text{theo}}$ ( $\mu\text{b}$ )	QF
Peak1	0.000 (1/2 <sup>+</sup> )	0.000 (3/2 <sup>-</sup> )	778	0.77	661	0.74	627	0.69
	0.110 (1/2 <sup>-</sup> )	0.000 (3/2 <sup>-</sup> )	141		248		235	
	0.197 (5/2 <sup>+</sup> )	0.000 (3/2 <sup>-</sup> )	6486		7139		6663	
Peak2	1.345 (5/2 <sup>-</sup> )	0.000 (3/2 <sup>-</sup> )		0.78	56	0.78	50	0.80
	1.458 (3/2 <sup>-</sup> )	0.000 (3/2 <sup>-</sup> )	<1		44		41	
	1.554 (3/2 <sup>+</sup> )	0.000 (3/2 <sup>-</sup> )	1672		2655		2434	
Peak3	0.000 (1/2 <sup>+</sup> )	2.124 (1/2 <sup>-</sup> )	70	0.53	68	0.80	63	0.73
	0.110 (1/2 <sup>-</sup> )	2.124 (1/2 <sup>-</sup> )	15		21		20	
	0.197 (5/2 <sup>+</sup> )	2.124 (1/2 <sup>-</sup> )	775		698		646	
	2.780 (9/2 <sup>+</sup> )	0.000 (3/2 <sup>-</sup> )			659		585	
Peak4	0.000 (1/2 <sup>+</sup> )	4.445 (5/2 <sup>-</sup> )		0.30	21	0.61	19	0.56
	0.110 (1/2 <sup>-</sup> )	4.445 (5/2 <sup>-</sup> )			12		11	
	0.197 (5/2 <sup>+</sup> )	4.445 (5/2 <sup>-</sup> )			147		137	
	2.780 (9/2 <sup>+</sup> )	2.124 (1/2 <sup>-</sup> )			86		78	
	0.000 (1/2 <sup>+</sup> )	5.020 (3/2 <sup>-</sup> )	21		26		24	
	0.110 (1/2 <sup>-</sup> )	5.020 (3/2 <sup>-</sup> )	6		9		8	
	0.197 (5/2 <sup>+</sup> )	5.020 (3/2 <sup>-</sup> )	308		359		333	

[42,43], where the contribution of transitions to individual states is difficult to be extracted. In the present case, where the light  $^{12}\text{C}$  target is used, the final level density is still manageable, allowing us to recognize several isolated structures in the populated spectra.

In particular, below the  $^{12}\text{B}$  one-neutron emission threshold ( $S_n = 3.370$  MeV), three structures are very pronounced. The first one corresponds to the transition to the isolated  $1_1^+$  ground states of  $^{18}\text{F}$  and  $^{12}\text{B}$ . The second peak is due to the unresolved transitions towards states of  $^{18}\text{F}$  at 0.937 ( $3_1^+$ ), 1.042 ( $0_1^+$ ), and 1.121 ( $5_1^+$ ) MeV, and of  $^{12}\text{B}$  at 0.953 ( $2_1^+$ ) MeV. In the charge-exchange studies of Refs. [42,44,45] it is found that, among the  $^{18}\text{F}$  states, the dominant one is the  $3^+$  state at 0.937 MeV. Peak 3 is due to the simultaneous excitation of the  $^{12}\text{B}$  ( $2_1^+$ ) state at 0.953 MeV leaving the  $^{18}\text{F}$  ejectile in its 0.937 ( $3_1^+$ ), 1.042 ( $0_1^+$ ), and 1.121 ( $5_1^+$ ) MeV states. Contributions from the transitions to the  $^{12}\text{B}$  states at 1.674 ( $2_1^-$ ) MeV and 2.621 ( $1_1^-$ ) MeV lie in the same region. However, looking at the shape of the third peak, their contribution is expected to be small.

Above  $S_n$ , peak 4 corresponds to the  $4^-$  resonance at 4.523 MeV of  $^{12}\text{B}$ , is expected to be strongly populated as already observed in other charge-exchange studies [44–46]. Peak 5 is likely originated by the simultaneous excitation of the  $^{12}\text{B}$  4.523 MeV state and the  $^{18}\text{F}$  ejectile excitations at 0.937 ( $3_1^+$ ), 1.042 ( $0_1^+$ ), and 1.121 ( $5_1^+$ ) MeV.

The detailed experimental and theoretical analysis of this reaction channel will be presented in a subsequent publication.

### III. THEORETICAL ANALYSIS

The theoretical analysis was performed in a multichannel approach. The aim is to provide a good description of the

complete network of nuclear reaction data both from the reaction and the structure calculation sides and in a fully consistent way.

In the case of elastic and inelastic scattering, the reaction calculations were performed in the optical model (OM), distorted wave Born approximation (DWBA), and coupled channels (CC) methods. The exact finite range (EFR) method implemented in the FRESKO code [47] was used to calculate the one-nucleon transfer cross sections in the DWBA, coupled channels Born approximation (CCBA), and coupled reaction channels (CRC) theoretical frameworks. The spectroscopic amplitudes were extracted within the large scale shell-model theoretical framework using the KSHELL code [48].

For a detailed analysis of the measured single-charge-exchange cross sections, both the one-step meson exchange and two-step nucleon transfer competitive mechanisms need to be evaluated and coherently added. Only the two-step mechanism refers to the same mean field degrees of freedom discussed and extracted in the present article. For the meson exchange part, supplementary information on the in-medium nucleon-nucleon isovector interaction is mandatory together with an adequate reaction model [11]. The complete analysis of the single-chargeexchange channel is beyond the scope of the present work and will be presented in a forthcoming paper, keeping the spirit of the multichannel approach here presented.

#### A. Initial-state interaction

The main ingredient of the initial-state interaction (ISI) is the optical potential (OP). Our analysis was performed using the São Paulo potential (SPP) [49]  $V_{\text{SPP}}(r)$  as the real and the

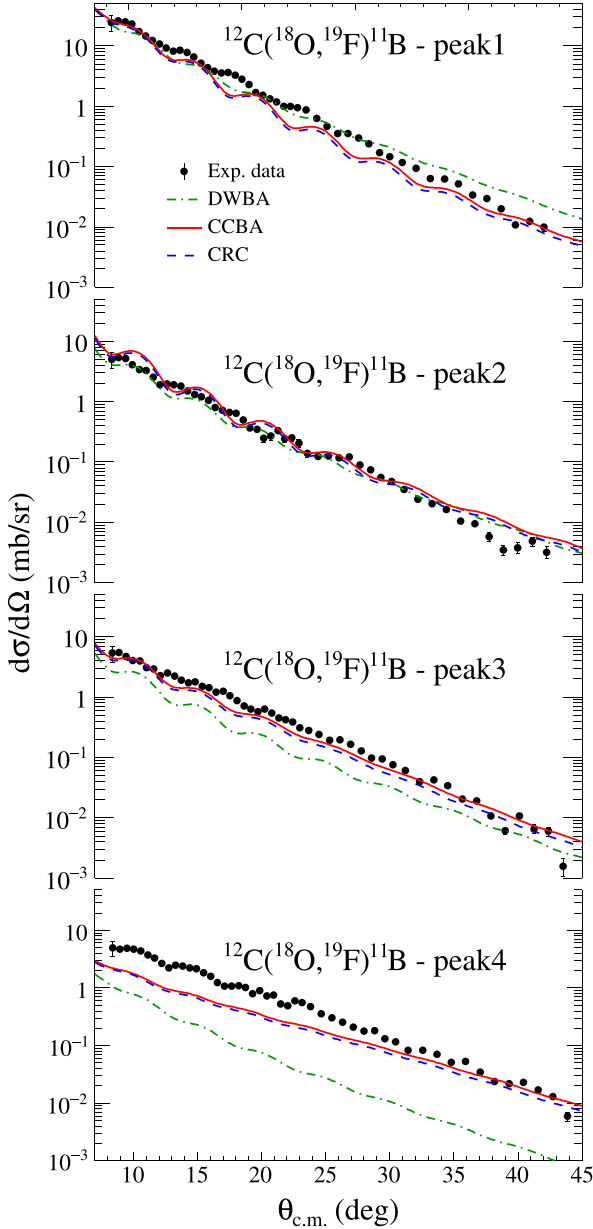


FIG. 5. Experimental cross-section angular distribution of the  $^{12}\text{C}(^{18}\text{O}, ^{19}\text{F})^{11}\text{B}$  one-proton pickup at 275 MeV of incident energy associated with the four peaks indicated in Fig. 1(c) and Table IV. Theoretical calculations of the one-proton pickup nuclear reaction for the DWBA, CCBA, and CRC approaches are shown with the green dot-dashed, continuous red, and blue dashed line, respectively.

imaginary parts of the OP:

$$U(r) = (N_R + iN_I)V_{\text{SPP}}(r), \quad (1)$$

where  $N_R$  and  $N_I$  are the real and imaginary strength factors, respectively. The assumptions on  $N_R$  and  $N_I$  values come from a wide application of the SPP to the description of experimental data [40,50–63]. Although the  $N_R$  value is always set to 1, the  $N_I$  one changes according to the coupling scheme adopted in the reaction calculations. Indeed, the imaginary part is introduced to account effectively for the absorption to reaction

channels and inelastic transitions, not explicitly introduced in the coupling scheme. In OM, where the only included channel in the coupling scheme is the elastic one,  $N_I$  is typically set to 0.78 [64]. The same holds also for the DWBA framework. If the couplings with the strongly populated inelastic scattering channels are explicitly taken into account, as in CC, CCBA, and CRC approaches, the  $N_I$  value is typically reduced to 0.6 [65]. Instead of playing with these parameters, even if this might lead to a better agreement with the data, we prefer to adopt the standard values, which are at least confirmed by a wide and robust literature [40,50–63].

The  $V_{\text{SPP}}(r)$  [49] comes from the double folding of a finite-range folding-type effective nucleon-nucleon interaction with the matter densities of the heavy nuclei involved in the collision. The nucleon-nucleon interaction is similar to the M3Y interaction of Refs. [66,67] in the surface region and contains an additional local-equivalent term given by an energy dependent strength factor to account for the Pauli nonlocality effects. The double folding is performed using two-parameter Fermi distributions for the matter density that is assumed to be spherical. The radius and diffuseness of the nuclear matter densities come from the systematic analysis of electron scattering data and Hartree-Fock-Bogoliubov calculations concerning a wide range of nuclei in the nuclear chart. Regarding the  $^{18}\text{O}$  diffuseness, it has been found [42,60,61,68–70] that it is reasonable to adopt a value of 0.61 fm (larger than the average value 0.56 fm of the SPP systematic) to account for the effect generated by the two valence neutrons bound to the  $^{16}\text{O}$  core.

The results of OM calculations for the  $^{18}\text{O} + ^{12}\text{C}$  elastic scattering at 275 MeV incident energy are shown in Fig. 2. The Fraunhofer diffraction pattern (Sommerfeld parameter  $\eta = 1.9$ ) is clearly visible in both experimental and theoretical angular distributions, and a good agreement is present for transferred momenta up to  $q \approx 2 \text{ fm}^{-1}$ . The discrepancy observed at larger  $q$  suggests the need to explicitly include the couplings with the first low-lying inelastic transitions, as already observed in similar studies [42,43,55,57,59,60]. This task is accomplished assuming a collective or a microscopic model with the proper coupling potentials.

In our approach, the  $2^+$  and  $3^-$  collective states of both projectile and target are introduced in the coupling scheme, as sketched in Fig. 6, and treated in terms of quadrupole and octupole excitations of the deformed  $^{18}\text{O}$  and  $^{12}\text{C}$  nuclei. The coupling potentials are defined in terms of multipole decomposition [4] of the main optical potential. The Coulomb  $V_C(r, \lambda)$  and nuclear  $V_N(r, \lambda)$  coupling potentials for the  $\lambda$  component were introduced in terms of the following definitions:

$$V_C(r, \lambda) = M(E\lambda)e^2 \frac{\sqrt{4\pi}}{2\lambda + 1} r^{-\lambda-1}, \quad (2a)$$

$$V_N(r, \lambda) = -\frac{\delta_\lambda}{\sqrt{4\pi}} \frac{dU(r)}{dr}. \quad (2b)$$

The Coulomb component of the deformed potential depends on the parameter  $M(E\lambda)$ , related to the reduced transition probability  $B(E\lambda; J \rightarrow J')$  for the electric operator  $E\lambda$  acting between the states  $J$  and  $J'$ , through the relation  $M(E\lambda) =$

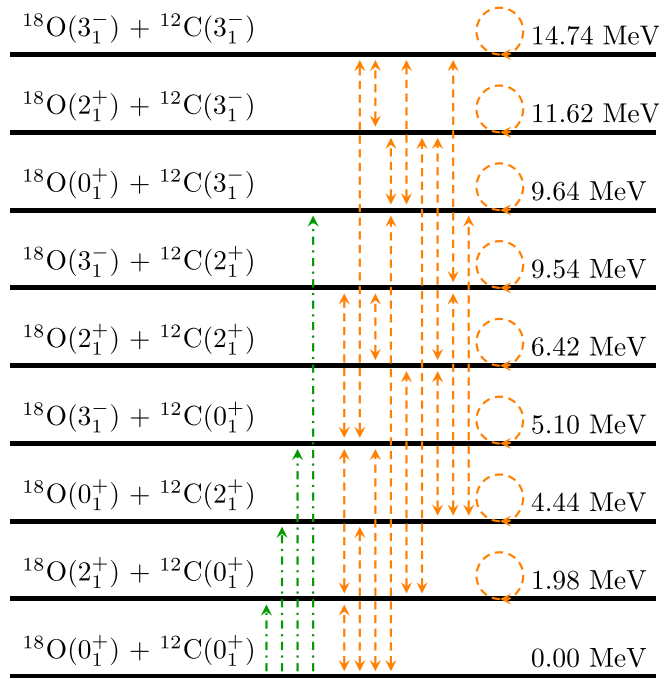


FIG. 6. Coupling scheme for the  $^{18}\text{O} + ^{12}\text{C}$  elastic and inelastic scattering. Couplings considered in the DWBA and CC calculations are indicated by the dot-dashed green and dashed orange arrows, respectively. Values on the right are the corresponding excitation energies.

$\pm\sqrt{(2J+1)B(E\lambda; J \rightarrow J')}$ . The sign is taken as that of the intrinsic quadrupole moment ( $\hat{Q}_0$ ), according to Ref. [47]. The nuclear component defined by Eq. (2b) is a complex deformed potential depending on the deformation length parameter  $\delta_\lambda$ . It is defined by the following formula:

$$\delta_\lambda = \beta_\lambda R_V = \frac{4\pi}{3Ze} \frac{M(E\lambda)}{R_V^{\lambda-1}}, \quad (3)$$

where  $B(E\lambda; J \rightarrow J')$  and the average radius of the potential  $R_V$  are involved. The same definitions for the Coulomb and nuclear deformations were recently applied in Refs. [40,42,43,59,60,62]. All the adopted values for the mentioned ingredients are listed in Table V. The DWBA and CC calculations were performed for the low-lying inelastic transitions adopting the coupling scheme shown in Fig. 6. The comparison between experimental data and theoretical calculations is shown in Fig. 3. The transitions included in the

DWBA approach correspond to the dot-dashed green arrows in Fig. 6. The population of the  $^{18}\text{O}(2_1^+) + ^{12}\text{C}(2_1^+)$  state is not allowed due to the lack of higher order terms in DWBA. Such effects, included in the CC approach (dashed orange arrows in Fig. 6) are responsible for the changes in the slopes observed comparing the DWBA and CC results shown in Fig. 3. A good description of the experimental data is reached using the CC approach. This is clearly visible also for the elastic scattering case (Fig. 2) in which the CC calculations very well reproduce both the oscillating pattern and the absolute value of the experimental cross-section angular distribution.

### B. One-nucleon transfer calculations

The main ingredients necessary to perform one-nucleon transfer calculations are the ISI and the final-state interaction (FSI), the proper description of single-particle wave functions and the residual potential responsible for the nuclear reaction. The ISI was discussed and defined in the previous section, from the analysis of the elastic and inelastic scattering experimental data. From the nuclear structure side, the single-particle wave functions and the spectroscopic amplitudes for the overlap between the initial and final states need to be properly introduced.

The single-particle wave functions for the nuclei involved in the one-nucleon transfer reactions were calculated considering the transferred particle bound to the core by means of a Woods-Saxon potential. For the  $^{17}\text{O} + n$  and  $^{18}\text{O} + p$  cases the adopted reduced radii and diffuseness are 1.26 and 0.7 fm, respectively. For the  $^{12}\text{C} + n$  and  $^{11}\text{B} + p$  the adopted values are 1.25 and 0.65 fm, respectively. These choices are consistent those recently presented in Refs. [39,40] in the case of similar systems and, more generally, are compatible with the typically adopted values [7]. The depth of the potential was adjusted to reproduce the separation energy of the transferred particle.

The spectroscopic amplitudes were computed within a large-scale shell-model formalism implemented in the KSHELL code [48]. The  $p$ - $sd$ -mod interaction [73] was used for both the projectile-like ( $^{18}\text{O}$ ,  $^{17}\text{O}$ ,  $^{19}\text{F}$ ) and the target-like ( $^{12}\text{C}$ ,  $^{13}\text{C}$ ,  $^{11}\text{B}$ ) nuclei. It is a modified version of the PSDWBT interaction [74] involving the full  $p$ - $sd$  valence subspace for protons and neutrons, assuming  $^4\text{He}$  as a closed core and  $1p_{3/2}$ ,  $1p_{1/2}$ ,  $1d_{5/2}$ ,  $2s_{1/2}$ , and  $1d_{3/2}$  valence orbits. In Table VII the comparison between the theoretical and experimental excitation energies of the states included in coupling schemes is shown. One can see a reasonably good agreement for all

TABLE V. Average radius  $R_V$  of the SPP, reduced transition probability  $B(E\lambda; J \rightarrow J')$ , reduced matrix element  $M(E\lambda)$ , and deformation length  $\delta_\lambda$  adopted for  $\lambda = 2, 3$  for the  $^{18}\text{O}$  and  $^{12}\text{C}$  nuclei.

	$R_V$ (fm)	$B(E2; 0^+ \rightarrow 2^+)$ ( $e^2\text{b}^2$ )	$M(E2)$ ( $e\text{fm}^2$ )	$\delta_2$ (fm)	$B(E3; 0^+ \rightarrow 3^-)$ ( $e^2\text{b}^3$ )	$M(E3)$ ( $e\text{fm}^3$ )	$\delta_3$ (fm)
$^{18}\text{O}$	3.13	0.0043 <sup>a</sup>	+6.56	+1.10	0.00046 <sup>b</sup>	+21.45	+1.15
$^{12}\text{C}$		0.00397 <sup>a</sup>	-6.30	-1.41	0.000257 <sup>c</sup>	-16.03	-1.14

<sup>a</sup>Pritychenko *et al.* [71].

<sup>b</sup>Kibedi and Spear [72].

<sup>c</sup>Itoh *et al.* [29].

the states. A reasonably good agreement is found for most of the states. Anyway, the limitations of the present calculations are expected to more significantly affect the energy spectra prediction than the wave function description [62]. In the initial partition the  $0^+$ ,  $2^+$ , and  $3^-$  states of both  $^{18}\text{O}$  and  $^{12}\text{C}$  nuclei were considered. The spectroscopic amplitudes related to the  $\langle ^{18}\text{O} | ^{17}\text{O} \rangle$  and  $\langle ^{13}\text{C} | ^{12}\text{C} \rangle$  overlaps for the one-neutron stripping case are listed in Tables VIII and IX of the Appendix, respectively. The spectroscopic amplitudes related to the  $\langle ^{19}\text{F} | ^{18}\text{O} \rangle$  and  $\langle ^{12}\text{C} | ^{11}\text{B} \rangle$  overlaps for the one-proton pick-up case are listed in Tables X and XI of the Appendix, respectively.

The FSI was introduced using the same SPP for the real and imaginary parts of the OPs. The radius and diffuseness of the matter densities nuclei were taken from the SPP systematics. As for the normalization factors, they were set as discussed in Sec. III A:  $N_I = 0.78$  for DWBA calculations and  $N_I = 0.6$  for CCBA ones, in which the couplings to the inelastic states also in the final partition were explicitly taken into account. The introduction of such couplings, including the reorientation terms, requires the use of the reduced matrix elements  $M(E\lambda)$  and  $\delta_\lambda$ . The  $M(E\lambda)$  values and signs were extracted from the same shell-model calculations for the  $\lambda = 2$  multipole and the  $\delta_2$  values were calculated according to Eq. (3). The obtained values are listed in Table VI together with the other relevant parameters. We found a good agreement between the calculated  $B(E2; J \rightarrow J')$  values and the available experimental data.

It is relevant to stress at this point that all the mentioned ingredients were introduced in a global fully comprehensive exact finite-range, prior, full complex remnant calculation including elastic and inelastic scattering and one-neutron and one-proton transfer in which all the cross sections are simultaneously calculated. This multichannel calculation is the first step for the complete description of the single-charge-exchange cross section.

The role of couplings with inelastic states in both the initial and final partitions and with the reaction channels was scrutinized comparing the DWBA, CCBA, and CRC approaches. The adopted coupling schemes are sketched in Fig. 7. In the DWBA calculations only the transitions from the ground state of the initial nuclei are taken into account (dot-dashed green arrows in Fig. 7) using one-way couplings, i.e., the couplings among different partitions are considered to the first order. The CCBA calculations also include the initial- and final-state inelastic couplings (dashed orange arrows in Fig. 7), thus allowing also the transitions from these states of the initial nuclei (dotted blue arrows in Fig. 7) in a one-way coupling. When the CRC calculations are performed, two-way couplings are introduced, which corresponds to taking into account couplings among different partitions up to the infinite order. The CRC coupling schemes are the same as the CCBA ones shown in Fig. 7.

The resulting theoretical calculations are compared to the experimental angular distributions in Figs. 4 and 5. In the one-proton pickup case, for the sake of a direct comparison of the theoretical cross sections to the experimental data, the

TABLE VI. Reduced matrix element  $M(E2)$  and deformation length  $\delta_2$  for selected transitions in the final partitions.

	Transition $J^\pi \longleftrightarrow J'^\pi$	Initial state (MeV)	Final state (MeV)	$M(E2)$ ( $e \text{ fm}^2$ )	$\delta_2$ (fm)	
$^{19}\text{F}$	$\frac{1}{2}^+ \longleftrightarrow \frac{5}{2}^+$	0.000	0.197	11.24	1.69	
	$\frac{1}{2}^+ \longleftrightarrow \frac{3}{2}^+$	0.000	1.554	-9.01	-1.35	
	$\frac{5}{2}^+ \longleftrightarrow \frac{5}{2}^+$	0.197	0.197	-12.90	-1.94	
	$\frac{5}{2}^+ \longleftrightarrow \frac{3}{2}^+$	0.197	1.554	6.73	1.01	
	$\frac{5}{2}^+ \longleftrightarrow \frac{9}{2}^+$	0.197	2.780	15.52	2.33	
	$\frac{3}{2}^+ \longleftrightarrow \frac{3}{2}^+$	1.554	1.554	-9.35	-1.40	
	$\frac{9}{2}^+ \longleftrightarrow \frac{9}{2}^+$	2.780	2.780	-16.71	-2.51	
	$\frac{1}{2}^- \longleftrightarrow \frac{5}{2}^-$	0.110	1.345	-18.90	-2.84	
	$\frac{1}{2}^- \longleftrightarrow \frac{3}{2}^-$	0.110	1.458	-16.19	-2.43	
	$\frac{5}{2}^- \longleftrightarrow \frac{3}{2}^-$	1.345	1.458	-9.73	-1.46	
	$\frac{5}{2}^- \longleftrightarrow \frac{5}{2}^-$	1.345	1.345	-19.16	-2.88	
	$\frac{3}{2}^- \longleftrightarrow \frac{3}{2}^-$	1.458	1.458	-15.31	-2.30	
	$^{17}\text{O}$	$\frac{5}{2}^+ \longleftrightarrow \frac{5}{2}^+$	0.000	0.000	-4.20	-0.71
		$\frac{5}{2}^+ \longleftrightarrow \frac{1}{2}^+$	0.000	0.871	3.56	0.60
$^{11}\text{B}$	$\frac{3}{2}^- \longleftrightarrow \frac{3}{2}^-$	0.000	0.000	5.93	1.60	
	$\frac{3}{2}^- \longleftrightarrow \frac{1}{2}^-$	0.000	2.124	3.55	0.96	
	$\frac{3}{2}^- \longleftrightarrow \frac{5}{2}^-$	0.000	4.444	8.30	2.24	
	$\frac{3}{2}^- \longleftrightarrow \frac{3}{2}^-$	0.000	5.020	-2.37	-0.64	
	$\frac{1}{2}^- \longleftrightarrow \frac{5}{2}^-$	2.124	4.444	-5.69	-1.54	
	$\frac{1}{2}^- \longleftrightarrow \frac{3}{2}^-$	2.124	5.020	-5.51	-1.49	
	$\frac{5}{2}^- \longleftrightarrow \frac{3}{2}^-$	4.444	5.020	5.43	1.47	
	$\frac{5}{2}^- \longleftrightarrow \frac{5}{2}^-$	4.444	4.444	0.41	0.11	
	$\frac{3}{2}^- \longleftrightarrow \frac{3}{2}^-$	5.020	5.020	-6.19	-1.67	
	$^{13}\text{C}$	$\frac{1}{2}^- \longleftrightarrow \frac{3}{2}^-$	0.000	3.684	5.33	1.21
$\frac{1}{2}^- \longleftrightarrow \frac{5}{2}^-$		0.000	7.547	6.34	1.44	
$\frac{3}{2}^- \longleftrightarrow \frac{5}{2}^-$		3.684	7.547	-4.13	-0.94	
$\frac{3}{2}^- \longleftrightarrow \frac{3}{2}^-$		3.684	3.684	6.07	1.38	
$\frac{5}{2}^- \longleftrightarrow \frac{5}{2}^-$		7.547	7.547	8.28	1.88	
$\frac{1}{2}^+ \longleftrightarrow \frac{5}{2}^+$		3.089	3.854	4.34	0.98	
$\frac{1}{2}^+ \longleftrightarrow \frac{5}{2}^+$		3.089	6.864	-6.15	-1.39	
$\frac{1}{2}^+ \longleftrightarrow \frac{3}{2}^+$		3.089	7.686	0.91	0.21	
$\frac{5}{2}^+ \longleftrightarrow \frac{5}{2}^+$		3.854	3.854	-6.80	-1.54	
$\frac{5}{2}^+ \longleftrightarrow \frac{5}{2}^+$		3.854	6.864	-5.47	-1.24	
$\frac{5}{2}^+ \longleftrightarrow \frac{7}{2}^+$		3.854	7.492	-9.27	-2.10	
$\frac{5}{2}^+ \longleftrightarrow \frac{3}{2}^+$		3.854	7.686	4.35	0.99	
$\frac{5}{2}^+ \longleftrightarrow \frac{5}{2}^+$		6.864	6.864	5.77	1.31	
$\frac{5}{2}^+ \longleftrightarrow \frac{7}{2}^+$		6.864	7.492	-6.63	-1.50	
$\frac{5}{2}^+ \longleftrightarrow \frac{3}{2}^+$	6.864	7.686	-2.98	-0.67		
$\frac{7}{2}^+ \longleftrightarrow \frac{7}{2}^+$	7.492	7.492	-3.39	-0.77		
$\frac{7}{2}^+ \longleftrightarrow \frac{3}{2}^+$	7.492	7.686	1.88	0.43		
$\frac{3}{2}^+ \longleftrightarrow \frac{3}{2}^+$	7.686	7.686	-4.79	-1.09		

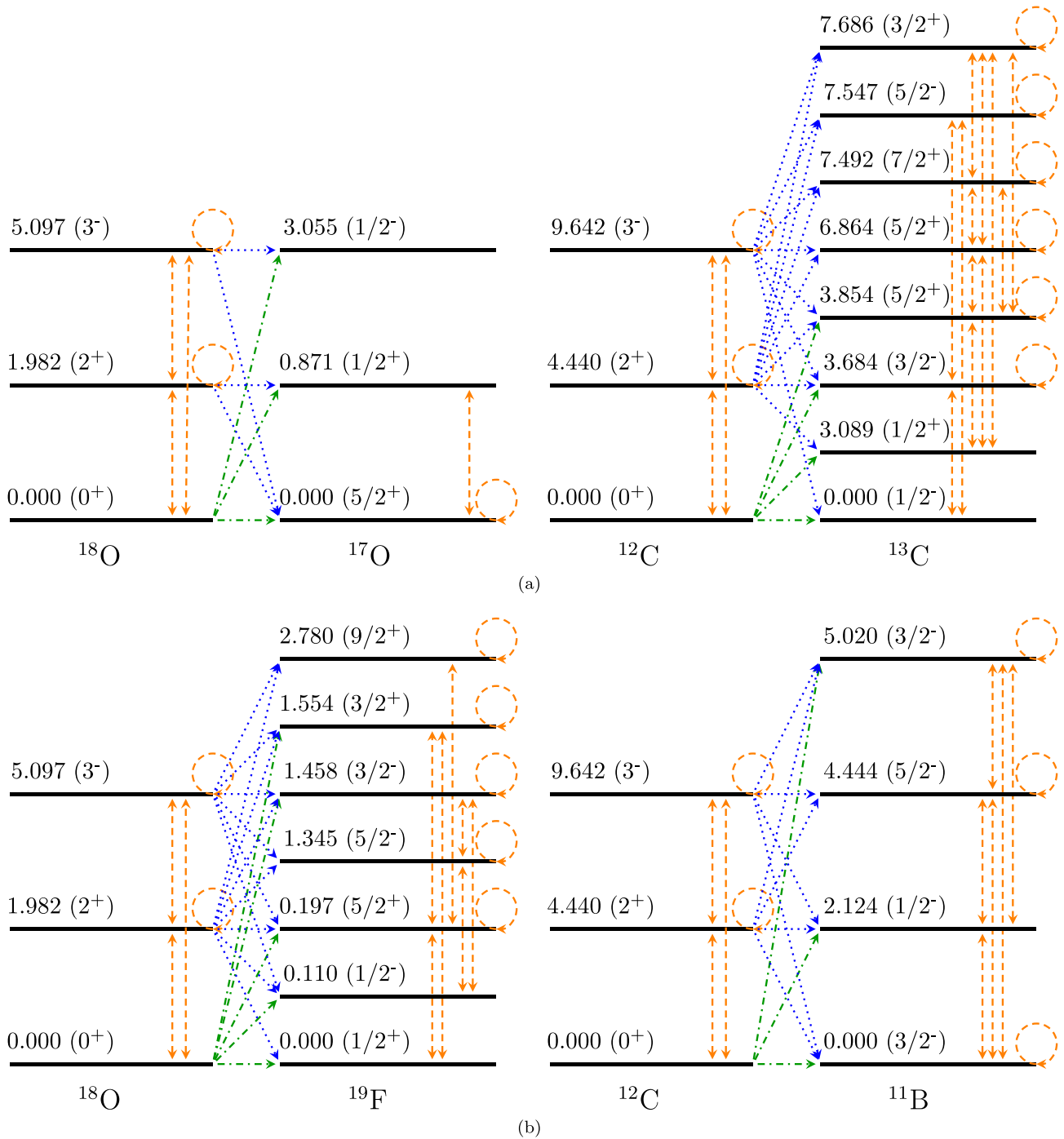


FIG. 7. Coupling schemes for the performed one-nucleon transfer calculations. Coupling schemes adopted for the one-neutron stripping and one-proton pick-up nuclear reactions are shown in (a) and (b), respectively. Couplings considered in the DWBA, CCBA, and CRC calculations are indicated by the dot-dashed green, dotted blue, and dashed orange arrows (see text for more information). Excitation energies (in MeV) and  $J^\pi$  of each of the involved states are also indicated.

theoretical curves shown in Fig. 5 are obtained by a weighted sum of the single transitions' differential cross sections. Weights were calculated by the integration in the adopted experimental excitation energy ranges of the spectral distribution obtained considering a normal Gaussian function for each transition. Each Gaussian was centered at the excitation

energy of each specific transition and the width was assigned as the achieved experimental resolution, taking into account also the Doppler broadening enlargement, where present. The integrated theoretical cross sections are listed in Tables III and IV for the one-neutron stripping and one-proton pickup reactions, respectively.

#### IV. DISCUSSION

In general, the theoretical calculations reasonably well reproduce the elastic and inelastic scattering and the one-nucleon transfer experimental data (see Figs. 2–5). In the one-neutron stripping case, the description is good even in the DWBA approach, showing that the role of couplings is not crucial and the analyzed final states are dominated by single-particle configurations. Instead, in the one-proton pickup case, the introduction of the couplings is mandatory to describe both the slope and the absolute cross section of the peaks 3 and 4. Also, exploratory CCBA calculations in which the couplings were introduced only in the initial partition improved the agreement with respect to the DWBA ones, but were not enough to satisfactorily reproduce the data. Thus, in the final CCBA calculations couplings in both partitions were introduced. Moving one step forward, the inclusion of couplings among different partition to infinite order (CRC) did not change the obtained results in both one-neutron and one-proton transfer cases.

To evaluate in a quantitative manner the agreement of the obtained theoretical results with the experimental data, the  $qf(\theta_i)$  quality factor was defined:

$$qf(\theta_i) = \frac{1}{1 + \left| \ln \frac{\sigma_{\text{theo}}(\theta_i)}{\sigma_{\text{exp}}(\theta_i)} \right|}, \quad (4)$$

where  $\sigma_{\text{exp}}$  and  $\sigma_{\text{theo}}$  are the measured and calculated values of the cross sections for the specific transition at the  $\theta_i$  scattering angle, respectively. The  $qf(\theta_i)$  values range between 0 and 1 corresponding to the worst and best agreements between the calculations and the experimental data, respectively. The proposed quality factor has the great advantage to weigh equally all the points of each angular distribution, regardless of their absolute value. This is a fundamental feature for distributions with an exponential slope, such as the differential cross section angular distributions. The  $qf(\theta_i)$  quantity was calculated for each  $i$  point of the experimental angular distributions in comparison to the respective values of each theoretical calculation (DWBA, CCBA, and CRC). Subsequently, the QF quantities were calculated for each analyzed angular distribution as an arithmetic average of the  $N_{\text{points}}$  measurements at different angles using the following formula:

$$QF = \frac{\sum_i qf(\theta_i)}{N_{\text{points}}}, \quad (5)$$

The QF values are listed in Tables II, III, and IV for each analyzed angular distribution and theoretical calculation. The reliability of the defined QF is confirmed by the values listed in Table II, in which for the elastic transition we see a change of 21% in the QF, from 0.63 obtained for DWBA to 0.76 for CCBA. This difference, which could appear small, is due to the fact that at forward angles both approaches are performing quite well. The big improvement in the description of the data with the CCBA approach is visible at large angles (see Fig. 2). In the case of the inelastic transition to the 4.44 MeV state of  $^{12}\text{C}$ , the best QF value is instead obtained in DWBA, since the oscillating pattern of the angular distribution is better described within this approach for this specific transition (see Fig. 3).

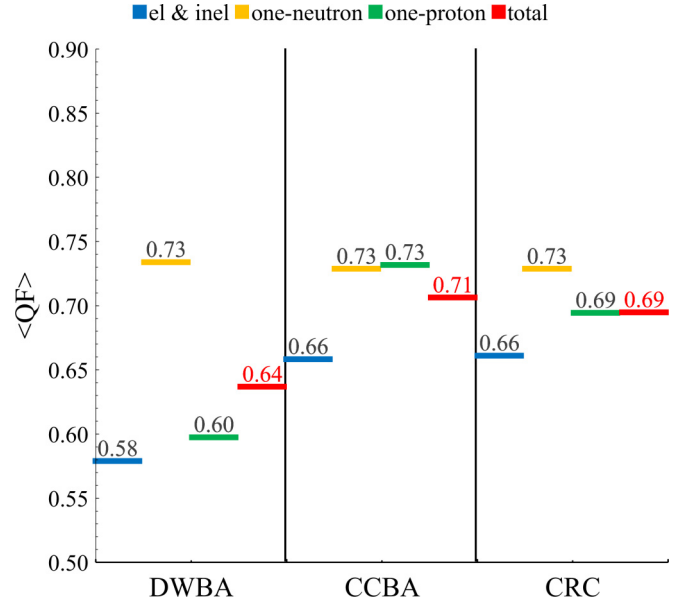


FIG. 8. Average quality factors extracted according to Eq. (5) in the experimentally explored angular range for the three analyzed channels (elastic/inelastic, one-neutron stripping, and one-proton pickup) and for the three theoretical approaches (DWBA, CCBA, and CRC) together with the total value (see text).

Finally, to evaluate the overall quality of the three different theoretical approaches, a unique  $\langle QF \rangle$  was extracted for each analyzed reaction channel through an average of the values reported in Tables II, III, and IV. The obtained results are shown in Fig. 8. In the same figure, also the  $\langle QF \rangle$  value corresponding to the whole data analysis is reported (total). It was evaluated as an average on the three analyzed reaction channels.

The results of this analysis, shown in Fig. 8, demonstrate that a significant improvement is achieved passing from the DWBA to the CCBA approach, without any significant breakthrough when the CRC effects are introduced. This result is a generalized confirmation of the crucial role played by the couplings among the states of the same partition in the fully comprehensive theoretical analysis of the nuclear reactions populated in the  $^{18}\text{O} + ^{12}\text{C}$  collision at 275 MeV.

#### V. CONCLUSIONS

The direct reactions induced by the collision of an  $^{18}\text{O}$  beam on a  $^{12}\text{C}$  target at 275 MeV incident energy were studied for the first time in a consistent multichannel approach from both the experimental and theoretical sides.

In particular, the  $^{12}\text{C}(^{18}\text{O}, ^{18}\text{O})^{12}\text{C}$  elastic and inelastic scattering, the  $^{12}\text{C}(^{18}\text{O}, ^{17}\text{O})^{13}\text{C}$  one-neutron stripping, the  $^{12}\text{C}(^{18}\text{O}, ^{19}\text{F})^{11}\text{B}$  one-proton pickup, and the  $^{12}\text{C}(^{18}\text{O}, ^{18}\text{F})^{12}\text{B}$  single-charge-exchange reactions were explored under the same experimental conditions. Energy spectra and absolute cross-section angular distributions were measured in a wide range at forward scattering angles. The achieved energy ( $\delta E_x \approx 0.6$  MeV) and angular ( $\delta\theta_{c.m.} \approx 0.5^\circ$ )

resolution allowed us to isolate specific transitions and to map the diffraction patterns in the angular distributions.

The experimental data were analyzed with state-of-the-art methods of quantum scattering theory at different levels of complexity, from the DWBA up to the CCBA and, further on, to the CRC schemes, where a large number of coupling channels was included in the model spaces. The initial (ISI) and final (FSI) state nucleus-nucleus interactions, adopted in the calculations, were taken from the double folded São Paulo potential for the real part. An imaginary potential was also included, as usual, to account for the average loss of flux towards more dissipative processes. Instead of fitting the optical potentials to the experimental data, we decided to follow a well-established prescription in which the imaginary potential is assumed to have the same geometry of the real part and a scaling factor is taken from a wide systematics. Thus, no free parameters adapted to this study come from the choice of the ISI and FSI. Nuclear structure inputs, necessary to model the different reaction channels under study, were extracted from large-scale shell-model calculations performed with well-established interactions, while keeping a high degree of consistency in the multichannel analysis.

A first conclusion is that the cross-section calculations describe very well the experimental data, both in terms of the absolute values and diffraction patterns for all the analyzed reaction channels, although the use of the mentioned systematics is not necessarily the best way to analyze the data. These results confirm the robustness of the adopted systematics. Surprisingly, we notice that DWBA calculations, which by definition do not account for the coupling to inelastic and transfer channels, prove to be quite accurate for all the studied channels. In general, better results are found when the couplings to inelastic transitions in both the entrance and exit partitions are introduced, as done in CCBA calculations. In contrast, no real improvement is found when the coupling scheme is extended to relevant transfer channels, as done in CRC calculations.

An attempt to perform a quantitative evaluation of the degree of agreement of the calculations with the data was performed through the introduction of a quality factor. To our knowledge a similar technique has never been used in the community. Typically, in papers where a comparison of cross-section angular distributions with calculations is presented, the comments about the agreement are based on qualitative considerations only. Sometimes, the reduced  $\chi^2$  values are evaluated, which, however, tend to overweight the points at forward angles characterized by the largest cross sections. Indeed, the main issue in the definition of the quality factor is due to the very broad range of cross sections spanning several orders of magnitude.

Our quality factor weighs all the data points equally, regardless of their absolute value and this is a great advantage for distributions with exponential slope spanning several orders of magnitude, such as the differential cross section angular distributions of heavy-ion quasielastic reactions. The adopted quality factor ranges from zero to unity, when moving from a complete disagreement to a full agreement. In our analysis the quality factor is found to be about 0.6 for DWBA calculations, rising to about 0.7 for CCBA and CRC

TABLE VII. Comparison between the experimental and theoretical low-lying spectra obtained by large scale shell-model calculations for the involved nuclei using the  $p$ - $sd$ -mod interaction [73]. Energies are in MeV.

	$J^\pi$	Experimental	Theoretical
$^{18}\text{O}$	$0_1^+$	0.000	0.000
	$2_1^+$	1.982	2.264
	$4_1^+$	3.554	3.620
	$0_2^+$	3.633	4.249
	$3_1^-$	5.097	4.929
$^{12}\text{C}$	$0_1^+$	0.000	0.000
	$2_1^+$	4.440	4.950
	$3_1^-$	9.641	8.127
$^{17}\text{O}$	$\frac{5}{2}_1^+$	0.000	0.000
	$\frac{1}{2}_1^+$	0.871	0.871
	$\frac{1}{2}_1^-$	3.055	3.538
$^{13}\text{C}$	$\frac{1}{2}_1^-$	0.000	0.000
	$\frac{1}{2}_1^+$	3.089	1.830
	$\frac{3}{2}_1^-$	3.684	3.509
	$\frac{5}{2}_1^+$	3.854	2.418
	$\frac{5}{2}_2^+$	6.864	6.164
	$\frac{7}{2}_1^+$	7.492	6.535
	$\frac{5}{2}_1^-$	7.547	7.537
$^{19}\text{F}$	$\frac{3}{2}_1^+$	7.686	6.706
	$\frac{1}{2}_1^+$	0.000	0.107
	$\frac{1}{2}_1^-$	0.110	0.744
	$\frac{5}{2}_1^+$	0.197	0.000
	$\frac{5}{2}_1^-$	1.345	2.422
	$\frac{3}{2}_1^-$	1.458	2.615
	$\frac{3}{2}_1^+$	1.554	1.080
	$\frac{9}{2}_1^+$	2.780	3.104
	$^{11}\text{B}$	$\frac{3}{2}_1^-$	0.000
$\frac{1}{2}_1^-$		2.124	1.689
$\frac{5}{2}_1^-$		4.444	4.666
$\frac{3}{2}_2^-$		5.020	4.654

ones, thus highlighting the actual improvements due to the inclusion of coupled channels in the scattering equations. It is interesting to notice that the quality factor presents similar values for different reaction channels when the calculation scheme is established, while significant changes are found when it is changed, e.g., when moving from DWBA to CCBA. This is not surprising, although quite significant, due to the strong consistency of the multichannel technique adopted here, which allows one to treat different reaction channels in very similar experimental conditions and theoretical schemes of approximations.

The multichannel approach discussed in this work is a very promising method for accurate investigations of direct

TABLE VIII. One-neutron spectroscopic amplitudes (SA) for the projectile overlaps using the  $p$ - $sd$ -mod interaction [73]. The symbols  $n$ ,  $l$ , and  $j$  correspond to the principal quantum number, the orbital, and the total angular momentum of the transferred neutron orbitals, respectively.

$^{18}\text{O}$		$^{17}\text{O}$			
$E_x$ (MeV)	$J_\pi$	$E_x$ (MeV)	$J_\pi$	$nl_j$	SA
0.000	$0^+$	0.000	$\frac{5}{2}^+$	$1d_{\frac{5}{2}}$	1.2708
		0.871	$\frac{1}{2}^+$	$2s_{\frac{1}{2}}$	-0.4345
		3.055	$\frac{1}{2}^-$	$1p_{\frac{1}{2}}$	-0.8155
1.982	$2^+$	0.000	$\frac{5}{2}^+$	$1d_{\frac{5}{2}}$	-1.0734
		0.000	$\frac{5}{2}^+$	$2s_{\frac{1}{2}}$	-0.5093
		0.000	$\frac{5}{2}^+$	$1d_{\frac{3}{2}}$	-0.0799
		0.871	$\frac{1}{2}^+$	$1d_{\frac{5}{2}}$	0.4994
		0.871	$\frac{1}{2}^+$	$1d_{\frac{3}{2}}$	0.1737
5.097	$3^-$	0.000	$\frac{5}{2}^+$	$1p_{\frac{1}{2}}$	-0.1135
		0.000	$\frac{5}{2}^+$	$1p_{\frac{3}{2}}$	0.0988
		0.871	$\frac{1}{2}^+$	$1d_{\frac{5}{2}}$	-0.2430
		3.055	$\frac{1}{2}^-$	$1d_{\frac{5}{2}}$	-0.2430

reactions stemming from heavy-ion collisions. The results found here also give the chance for future investigation on the quality of different nuclear structure models from heavy-ion direct reactions. In the present article, we focused on the nuclear reaction aspect of the multichannel approach, probing it by a robust nuclear structure model. Investigating different nuclear structure models is an interesting research program that goes beyond the scope of this work and will be pursued in the future. This perspective is quite appealing for high precision nuclear spectroscopy of heavy nuclei as recently proposed in many areas of nuclear physics. An example is the NUMEN project with its challenging goal to provide valuable information on nuclear states involved in neutrino-less double beta decay from single- and double-charge-exchange cross sections. What we do in the present work is quite different from what is typically found in literature for the analyses of heavy-ion direct nuclear reactions. The multichannel approach puts a strong interconnection among a wide set of data, stemming from the same collision. The novelty here is in the significant widening of the model space explored consistently both in the experiment and in the theoretical analysis. In general, the more channels, the harder is the challenge and the safer is the result in case of successful description of the data. For example, studying only neutron transfer reactions probes mostly the neutron shell structure, giving almost no information on the proton side. Studying transitions in different excitation energy regions and reaction channels could require the activation of different orbits in the model space. In this way, the multichannel approach has the advantage to probe consistently various aspects of the nuclear many-body states. We believe that such multichannel approach is mandatory

TABLE IX. One-neutron spectroscopic amplitudes (SA) for the target overlaps using the  $p$ - $sd$ -mod interaction [73]. The symbols  $n$ ,  $l$ , and  $j$  correspond to the principal quantum number, the orbital, and the total angular momentum of the transferred neutron orbitals, respectively.

$^{12}\text{C}$		$^{13}\text{C}$					
$E_x$ (MeV)	$J^\pi$	$E_x$ (MeV)	$J^\pi$	$nl_j$	SA		
0.000	$0^+$	0.000	$\frac{1}{2}^-$	$1p_{\frac{1}{2}}$	0.8025		
		3.089	$\frac{1}{2}^+$	$2s_{\frac{1}{2}}$	0.8962		
		3.684	$\frac{3}{2}^-$	$1p_{\frac{3}{2}}$	-0.3601		
		3.854	$\frac{5}{2}^+$	$1d_{\frac{5}{2}}$	-0.9099		
		4.440	$2^+$	0.000	$\frac{1}{2}^-$	$1p_{\frac{3}{2}}$	-0.9948
				3.089	$\frac{1}{2}^+$	$1d_{\frac{3}{2}}$	-0.0393
				3.089	$\frac{1}{2}^+$	$1d_{\frac{5}{2}}$	0.3112
				3.684	$\frac{3}{2}^-$	$1p_{\frac{1}{2}}$	-0.8205
				3.684	$\frac{3}{2}^-$	$1p_{\frac{3}{2}}$	0.5404
				3.854	$\frac{5}{2}^+$	$1d_{\frac{3}{2}}$	0.0588
				3.854	$\frac{5}{2}^+$	$1d_{\frac{5}{2}}$	-0.1982
				3.854	$\frac{5}{2}^+$	$2s_{\frac{1}{2}}$	-0.1105
				6.864	$\frac{3}{2}^+$	$1d_{\frac{3}{2}}$	-0.0414
				6.864	$\frac{3}{2}^+$	$1d_{\frac{5}{2}}$	-0.6310
		6.864	$\frac{5}{2}^+$	$2s_{\frac{1}{2}}$	0.7015		
7.492	$\frac{7}{2}^+$	$1d_{\frac{3}{2}}$	-0.0040				
7.492	$\frac{7}{2}^+$	$1d_{\frac{5}{2}}$	-0.8570				
7.547	$\frac{5}{2}^-$	$1p_{\frac{1}{2}}$	-0.5441				
7.547	$\frac{5}{2}^-$	$1p_{\frac{3}{2}}$	-0.2146				
7.686	$\frac{3}{2}^+$	$1d_{\frac{3}{2}}$	-0.2283				
7.686	$\frac{3}{2}^+$	$1d_{\frac{5}{2}}$	-0.5145				
7.686	$\frac{3}{2}^+$	$2s_{\frac{1}{2}}$	0.1059				
9.641	$3^-$	0.000	$\frac{1}{2}^-$	$1d_{\frac{5}{2}}$	0.1371		
		3.089	$\frac{1}{2}^+$	$1d_{\frac{3}{2}}$	-0.0085		
		3.684	$\frac{3}{2}^-$	$1d_{\frac{5}{2}}$	0.2771		
		3.684	$\frac{3}{2}^-$	$1d_{\frac{3}{2}}$	0.0222		
		3.854	$\frac{5}{2}^+$	$1p_{\frac{1}{2}}$	-0.5466		
		3.854	$\frac{5}{2}^+$	$1p_{\frac{3}{2}}$	0.0718		
		6.864	$\frac{5}{2}^+$	$1p_{\frac{1}{2}}$	-0.1230		
		6.864	$\frac{5}{2}^+$	$1p_{\frac{3}{2}}$	-0.4395		
		7.492	$\frac{7}{2}^+$	$1p_{\frac{1}{2}}$	0.5076		
		7.492	$\frac{7}{2}^+$	$1d_{\frac{3}{2}}$	0.0284		
		7.547	$\frac{5}{2}^-$	$1d_{\frac{5}{2}}$	-0.1507		
		7.547	$\frac{5}{2}^-$	$2s_{\frac{1}{2}}$	0.0288		
7.686	$\frac{3}{2}^+$	$1p_{\frac{3}{2}}$	-0.4286				

for the purposes of studying the DCE reactions and that, in general, it is a powerful approach to keep under control all the degrees of freedom in the theoretical data analysis.

TABLE X. One-proton spectroscopic amplitudes (SA) for the projectile overlaps using the  $p$ - $sd$ -mod interaction [73]. The symbols  $n$ ,  $l$ , and  $j$  correspond to the principal quantum number, the orbital, and the total angular momentum of the transferred neutron orbitals, respectively.

$^{18}\text{O}$		$^{19}\text{F}$				
$E_x$ (MeV)	$J^\pi$	$E_x$ (MeV)	$J^\pi$	$nl_j$	SA	
0.000	$0^+$	0.000	$\frac{1}{2}^+$	$2s_{\frac{1}{2}}$	-0.5539	
		0.110	$\frac{1}{2}^-$	$1p_{\frac{1}{2}}$	-0.2444	
		0.197	$\frac{5}{2}^+$	$1d_{\frac{5}{2}}$	0.6644	
		1.345	$\frac{5}{2}^-$			
		1.458	$\frac{3}{2}^-$	$1p_{\frac{3}{2}}$	-0.0106	
		1.554	$\frac{3}{2}^+$	$1d_{\frac{3}{2}}$	-0.4238	
		2.780	$\frac{9}{2}^+$			
		1.982	$2^+$	0.000	$\frac{1}{2}^+$	$1d_{\frac{5}{2}}$
0.000	$\frac{1}{2}^+$	$1d_{\frac{3}{2}}$		-0.2806		
0.110	$\frac{1}{2}^-$	$1p_{\frac{3}{2}}$		-0.0301		
0.197	$\frac{5}{2}^+$	$1d_{\frac{5}{2}}$		-0.4265		
0.197	$\frac{5}{2}^+$	$2s_{\frac{1}{2}}$		-0.3113		
0.197	$\frac{5}{2}^+$	$1d_{\frac{3}{2}}$		0.1563		
1.345	$\frac{5}{2}^-$	$1p_{\frac{3}{2}}$		0.0186		
1.345	$\frac{5}{2}^-$	$1p_{\frac{1}{2}}$		0.1366		
1.458	$\frac{3}{2}^-$	$1p_{\frac{3}{2}}$		-0.0022		
1.458	$\frac{3}{2}^-$	$1p_{\frac{1}{2}}$		0.1639		
1.554	$\frac{3}{2}^+$	$1d_{\frac{5}{2}}$		0.3146		
1.554	$\frac{3}{2}^+$	$2s_{\frac{1}{2}}$		0.3539		
1.554	$\frac{3}{2}^+$	$1d_{\frac{3}{2}}$		0.3185		
2.780	$\frac{9}{2}^+$	$1d_{\frac{5}{2}}$		0.7872		
5.097	$3^-$	0.000		$\frac{1}{2}^+$		
		0.110		$\frac{1}{2}^-$	$1d_{\frac{5}{2}}$	-0.4906
		0.197	$\frac{5}{2}^+$	$1p_{\frac{1}{2}}$	0.5849	
		0.197	$\frac{5}{2}^+$	$1p_{\frac{3}{2}}$	-0.0900	
		1.345	$\frac{5}{2}^-$	$1d_{\frac{3}{2}}$	-0.0268	
		1.345	$\frac{5}{2}^-$	$1d_{\frac{5}{2}}$	-0.4864	
		1.345	$\frac{5}{2}^-$	$2s_{\frac{1}{2}}$	-0.3768	
		1.458	$\frac{3}{2}^-$	$1d_{\frac{3}{2}}$	0.0486	
		1.458	$\frac{3}{2}^-$	$1d_{\frac{5}{2}}$	0.2614	
		1.554	$\frac{3}{2}^+$	$1p_{\frac{3}{2}}$	0.1675	
		2.780	$\frac{9}{2}^+$	$1p_{\frac{3}{2}}$	-0.0787	

In a forthcoming publication, all the methods presented and discussed here will be used for the analysis of the  $^{12}\text{C}(^{18}\text{O}, ^{18}\text{F})^{12}\text{B}$  single-charge-exchange reaction, where the meson exchange mechanism will be consistently introduced for the first time in the same coupled channel framework, together with the nucleon transfer charge-exchange mechanism discussed here.

TABLE XI. One-proton spectroscopic amplitudes (SA) for the target overlaps using the  $p$ - $sd$ -mod interaction [73]. The symbols  $n$ ,  $l$ , and  $j$  correspond to the principal quantum number, the orbital, and the total angular momentum of the transferred neutron orbitals, respectively.

$^{12}\text{C}$		$^{11}\text{B}$					
$E_x$ (MeV)	$J^\pi$	$E_x$ (MeV)	$J^\pi$	$nl_j$	SA		
0.000	$0^+$	0.000	$\frac{3}{2}^-$	$1p_{\frac{3}{2}}$	1.7239		
		2.124	$\frac{1}{2}^-$	$1p_{\frac{1}{2}}$	0.6520		
		4.444	$\frac{5}{2}^-$				
		5.020	$\frac{3}{2}^-$	$1p_{\frac{3}{2}}$	0.5131		
		4.440	$2^+$	0.000	$\frac{3}{2}^-$	$1p_{\frac{1}{2}}$	0.6607
		0.000		$\frac{3}{2}^-$	$1p_{\frac{3}{2}}$	-0.0733	
		2.124		$\frac{1}{2}^-$	$1p_{\frac{3}{2}}$	-0.5802	
		4.444		$\frac{5}{2}^-$	$1p_{\frac{1}{2}}$	0.3768	
4.444	$\frac{5}{2}^-$	$1p_{\frac{3}{2}}$		1.0979			
5.020	$\frac{3}{2}^-$	$1p_{\frac{1}{2}}$		-0.2434			
5.020	$\frac{3}{2}^-$	$1p_{\frac{3}{2}}$		0.7902			
9.641	$3^-$	0.000		$\frac{3}{2}^-$	$1d_{\frac{3}{2}}$	-0.2374	
0.000		$\frac{3}{2}^-$	$1d_{\frac{5}{2}}$	-0.4559			
2.124		$\frac{1}{2}^-$	$1d_{\frac{3}{2}}$	0.2820			
4.444		$\frac{5}{2}^-$	$1d_{\frac{3}{2}}$	0.1858			
4.444		$\frac{5}{2}^-$	$1d_{\frac{5}{2}}$	0.2286			
4.444		$\frac{5}{2}^-$	$2s_{\frac{1}{2}}$	0.0022			
5.020		$\frac{3}{2}^-$	$1d_{\frac{3}{2}}$	-0.2697			
5.020		$\frac{3}{2}^-$	$1d_{\frac{5}{2}}$	0.0500			

## ACKNOWLEDGMENTS

The authors would like to thank all the staff of the LNS Accelerator for the support during the experiments. This project received funding from the European Research Council (ERC) under the European Union's Horizon 2020 research and innovation program (Grant Agreement No. 714625). The NUMEN project is mainly funded by INFN. Support from the Brazilian funding agencies FAPESP, Proc. No. 2019/07767-1, and INCT-FNA, Proc. No. 464898/2014-5, is acknowledged. The Mexican authors received funding from DGAPA-UNAM IN107820, IG101120 and CONACYT315839 projects.

## APPENDIX: TABLES OF SPECTROSCOPIC AMPLITUDES

In Tables VII–XI, the comparisons between the experimental and theoretical spectra obtained by the large scale shell-model calculations are reported. The spectroscopic amplitudes used in the performed reaction calculations for the involved nuclei are also listed. The values of the theoretical excitation energies and the spectroscopic amplitudes are obtained by the KSHELL [48] software using the  $p$ - $sd$ -mod interaction [73] (see Sec. III B).

- [1] F. Cappuzzello, H. Lenske, M. Cavallaro, C. Agodi, N. Auerbach, J. Bellone, R. Bijker, S. Burrello, S. Calabrese, D. Carbone, M. Colonna, G. De Gregorio, J. Ferreira, D. Gambacurta, H. García-Tecocoatzi, A. Gargano, J. Lay, R. Linares, J. Lubian, E. Santopinto *et al.*, Shedding light on nuclear aspects of neutrinoless double beta decay by heavy-ion double charge exchange reactions, *Prog. Part. Nucl. Phys.* **128**, 103999 (2023).
- [2] T. Aumann, C. Barbieri, D. Bazin, C. Bertulani, A. Bonaccorso, W. Dickhoff, A. Gade, M. Gómez-Ramos, B. Kay, A. Moro, T. Nakamura, A. Obertelli, K. Ogata, S. Paschalis, and T. Uesaka, Quenching of single-particle strength from direct reactions with stable and rare-isotope beams, *Prog. Part. Nucl. Phys.* **118**, 103847 (2021).
- [3] F. Cappuzzello, D. Carbone, M. Cavallaro, M. Bondi, C. Agodi, F. Azaiez, A. Bonaccorso, A. Cunsolo, L. Fortunato, A. Foti, S. Franchoo, E. Khan, R. Linares, J. Lubian, J. Scarpaci, and A. Vitturi, Signatures of the giant pairing vibration in the  $^{14}\text{C}$  and  $^{15}\text{C}$  atomic nuclei, *Nat. Commun.* **6**, 6743 (2015).
- [4] G. Satchler, *Direct Nuclear Reactions*, International Series of Monographs on Physics Vol. 68 (Clarendon, Oxford, 1983).
- [5] N. K. Glendenning, *Direct Nuclear Reactions* (Academic, New York, 1983).
- [6] L. Canto, P. Gomes, R. Donangelo, J. Lubian, and M. Hussein, Recent developments in fusion and direct reactions with weakly bound nuclei, *Phys. Rep.* **596**, 1 (2015).
- [7] N. Anyas-Weiss, J. Cornell, P. Fisher, P. Hudson, A. Menchaca-Rocha, D. Millener, A. Panagiotou, D. Scott, D. Strottman, D. Brink, B. Buck, P. Ellis, and T. Engeland, Nuclear structure of light nuclei using the selectivity of high energy transfer reactions with heavy ions, *Phys. Rep.* **12**, 201 (1974).
- [8] S. Kahana and A. J. Baltz, One- and Two-Nucleon Transfer Reactions with Heavy Ions, in *Advances in Nuclear Physics*, edited by M. Baranger and E. Vogt (Springer, Boston, 1977), pp. 1–122.
- [9] D. Frekers, P. Puppe, J. Thies, and H. Ejiri, Gamow–Teller strength extraction from ( $^3\text{He}, t$ ) reactions, *Nucl. Phys. A* **916**, 219 (2013).
- [10] H. Ejiri, J. Suhonen, and K. Zuber, Neutrino–nuclear responses for astro-neutrinos, single beta decays and double beta decays, *Phys. Rep.* **797**, 1 (2019).
- [11] H. Lenske, F. Cappuzzello, M. Cavallaro, and M. Colonna, Heavy ion charge exchange reactions as probes for nuclear  $\beta$ -decay, *Prog. Part. Nucl. Phys.* **109**, 103716 (2019).
- [12] F. Cappuzzello, M. Cavallaro, C. Agodi, M. Bondi, D. Carbone, A. Cunsolo, and A. Foti, Heavy-ion double charge exchange reactions: A tool toward  $0\nu\beta\beta$  nuclear matrix elements, *Eur. Phys. J. A* **51**, 145 (2015).
- [13] N. Shimizu, J. Menéndez, and K. Yako, Double Gamow-Teller Transitions and its Relation to Neutrinoless  $\beta\beta$  Decay, *Phys. Rev. Lett.* **120**, 142502 (2018).
- [14] F. Cappuzzello *et al.*, The NUMEN project: Nuclear matrix elements for neutrinoless double beta decay, *Eur. Phys. J. A* **54**, 72 (2018).
- [15] H. Ejiri, Single- and double-charge exchange reactions and nuclear matrix element for double-beta decay, *Universe* **8**, 457 (2022).
- [16] A. Pakou, O. Sgouros, V. Soukeras, and F. Cappuzzello, Global descriptions and decay rates for continuum excitation of weakly bound nuclei, *Eur. Phys. J. A* **57**, 25 (2021).
- [17] F. Cappuzzello, D. Carbone, M. Cavallaro, A. Spatafora, J. Ferreira, C. Agodi, R. Linares, and J. Lubian, Confirmation of giant pairing vibration evidence in  $^{12,13}\text{C}(^{18}\text{O}, ^{16}\text{O})^{14,15}\text{C}$  reactions at 275 mev, *Eur. Phys. J. A* **57**, 34 (2021).
- [18] A. Spatafora, A full-comprehensive experimental and theoretical approach applied to the  $^{12}\text{C}(^{18}\text{O}, ^{18}\text{F})^{12}\text{B}$  single charge-exchange reaction at 15.3 AMeV, *IL Nuovo Cimento C* **45**, 131 (2022).
- [19] F. Cappuzzello, C. Agodi, D. Carbone, and M. Cavallaro, The MAGNEX spectrometer: results and perspectives, *Eur. Phys. J. A* **52**, 167 (2016).
- [20] M. Cavallaro, F. Cappuzzello, D. Carbone, A. Cunsolo, A. Foti, A. Khouaja, M. R. D. Rodrigues, J. S. Winfield, and M. Bondi, The low-pressure focal plane detector of the MAGNEX spectrometer, *Eur. Phys. J. A* **48**, 59 (2012).
- [21] D. Torresi, O. Sgouros, V. Soukeras, M. Cavallaro, F. Cappuzzello, D. Carbone, C. Agodi, G. Brischetto, S. Calabrese, I. Ciraldo, N. Deshmukh, A. Hacisalihoglu, L. L. Fauci, and A. Spatafora, An upgraded focal plane detector for the magnex spectrometer, *Nucl. Instrum. Methods Phys. Res., Sect. A* **989**, 164918 (2021).
- [22] F. Cappuzzello, M. Cavallaro, A. Cunsolo, A. Foti, D. Carbone, S. E. A. Orrigo, and M. R. D. Rodrigues, A particle identification technique for large acceptance spectrometers, *Nucl. Instrum. Methods Phys. Res., Sect. A* **621**, 419 (2010).
- [23] S. Calabrese *et al.*, First measurement of the  $^{116}\text{Cd}(^{20}\text{Ne}, ^{20}\text{O})^{116}\text{Sn}$  reaction at 15 A MeV, in *Proceedings, 35th Mazurian Lakes Conference on Physics: Exotic Nuclei - Laboratories for Fundamental Laws of Nature, Piaski, Poland, September 3–9, 2017* [Acta Phys. Pol. B **49**, 275 (2018)].
- [24] A. Badalà, M. La Cognata, R. Nania, M. Osipenko, S. Piantelli, R. Turrisi, L. Barion, S. Capra, D. Carbone, F. Carnesecchi, E. Casula, C. Chatterjee, G. Ciani, R. Depalo, A. Di Nitto, A. Fantini, A. Goasduff, G. Guardo, A. Kraan, A. Manna *et al.*, Trends in particle and nuclei identification techniques in nuclear physics experiments, *Riv. Nuovo Cimento* **45**, 189 (2022).
- [25] S. Calabrese, F. Cappuzzello, D. Carbone, M. Cavallaro, C. Agodi, D. Torresi, L. Acosta, D. Bonanno, D. Bongiovanni, T. Borello-Lewin, I. Boztosun, G. Brischetto, D. Calvo, I. Ciraldo, N. Deshmukh, P. de Faria, P. Finocchiaro, A. Foti, G. Gallo, A. Hacisalihoglu *et al.*, Analysis of the background on cross section measurements with the MAGNEX spectrometer: The ( $^{20}\text{Ne}, ^{20}\text{O}$ ) double charge exchange case, *Nucl. Instrum. Methods Phys. Res., Sect. A* **980**, 164500 (2020).
- [26] F. Cappuzzello, D. Carbone, and M. Cavallaro, Measuring the ions momentum vector with a large acceptance magnetic spectrometer, *Nucl. Instrum. Methods Phys. Res., Sect. A* **638**, 74 (2011).
- [27] D. Carbone, Signals of the giant pairing vibration in  $^{14}\text{C}$  and  $^{15}\text{C}$  nuclei populated by ( $^{18}\text{O}, ^{16}\text{O}$ ) two-neutron transfer reactions, *Eur. Phys. J. Plus* **130**, 143 (2015).
- [28] M. Freer, H. Fujita, Z. Buthelezi, J. Carter, R. W. Fearick, S. V. Förtsch, R. Neveling, S. M. Perez, P. Papka, F. D. Smit, J. A. Swartz, and I. Usman,  $2^+$  excitation of the  $^{12}\text{C}$  Hoyle state, *Phys. Rev. C* **80**, 041303(R) (2009).
- [29] M. Itoh, H. Akimune, M. Fujiwara, U. Garg, N. Hashimoto, T. Kawabata, K. Kawase, S. Kishi, T. Murakami, K. Nakanishi, Y. Nakatsugawa, B. K. Nayak, S. Okumura, H. Sakaguchi, H. Takeda, S. Terashima, M. Uchida, Y. Yasuda, M. Yosoi, and J. Zenihiro, Candidate for the  $2^+$  excited Hoyle state at  $E_x \sim 10$  MeV in  $^{12}\text{C}$ , *Phys. Rev. C* **84**, 054308 (2011).

- [30] D. Tilley, H. Weller, C. Cheves, and R. Chasteler, Energy levels of light nuclei  $A = 18-19$ , *Nucl. Phys. A* **595**, 1 (1995).
- [31] J. Kelley, J. Purcell, and C. Sheu, Energy levels of light nuclei  $A=12$ , *Nucl. Phys. A* **968**, 71 (2017).
- [32] M. Cavallaro, F. Cappuzzello, M. Bondi, D. Carbone, V. N. Garcia, A. Gargano, S. M. Lenzi, J. Lubian, C. Agodi, F. Azaiez, M. De Napoli, A. Foti, S. Franchoo, R. Linares, D. Nicolosi, M. Niikura, J. A. Scarpaci, and S. Tropea, Quantitative analysis of two-neutron correlations in the  $^{12}\text{C}(^{18}\text{O}, ^{16}\text{O})^{14}\text{C}$  reaction, *Phys. Rev. C* **88**, 054601 (2013).
- [33] D. Brink, Kinematical effects in heavy-ion reactions, *Phys. Lett. B* **40**, 37 (1972).
- [34] H. Ohnuma, N. Hoshino, O. Mikoshiba, K. Raywood, A. Sakaguchi, G. Shute, B. Spicer, M. Tanaka, M. Tanifuji, T. Terasawa, and M. Yasue, The  $^{12}\text{C}(d, p)^{13}\text{C}$  reaction at  $E_d = 30$  MeV and positive-parity states in  $^{13}\text{C}$ , *Nucl. Phys. A* **448**, 205 (1986).
- [35] D. Tilley, H. Weller, and C. Cheves, Energy levels of light nuclei  $A = 16-17$ , *Nucl. Phys. A* **564**, 1 (1993).
- [36] F. Ajzenberg-Selove, Energy levels of light nuclei  $A = 13-15$ , *Nucl. Phys. A* **523**, 1 (1991).
- [37] H. G. Pugh, D. L. Hendrie, M. Chabre, and E. Boschitz, High-resolution study of the reaction  $\text{C}^{12}(p, 2p)\text{B}^{11}$  at 50 MeV, *Phys. Rev. Lett.* **14**, 434 (1965).
- [38] G. Van Der Steenhoven, H. Blok, E. Jans, L. Lapikás, E. Quint, and P. De Witt Huberts, Weak transitions in the quasi-elastic reaction  $^{12}\text{C}(e, e'p)^{11}\text{B}$ , *Nucl. Phys. A* **484**, 445 (1988).
- [39] O. Sgouros, M. Cavallaro, F. Cappuzzello, D. Carbone, C. Agodi, A. Gargano, G. De Gregorio, C. Altana, G. A. Brischetto, S. Burrello, S. Calabrese, D. Calvo, V. Capirossi, E. R. Chávez Lomelí, I. Ciraldo, M. Cutuli, F. Delaunay, H. Djapo, C. Eke, P. Finocchiaro *et al.* (for the NUMEN Collaboration), One-proton transfer reaction for the  $^{18}\text{O} + ^{48}\text{Ti}$  system at 275 MeV, *Phys. Rev. C* **104**, 034617 (2021).
- [40] S. Calabrese, M. Cavallaro, D. Carbone, F. Cappuzzello, C. Agodi, S. Burrello, G. De Gregorio, J. L. Ferreira, A. Gargano, O. Sgouros, L. Acosta, P. Amador-Valenzuela, J. I. Bellone, T. Borello-Lewin, G. A. Brischetto, D. Calvo, V. Capirossi, E. R. Chávez Lomelí, I. Ciraldo, M. Colonna *et al.*,  $^{18}\text{O}$ -induced single-nucleon transfer reactions on  $^{40}\text{Ca}$  at 15.3A MeV within a multichannel analysis, *Phys. Rev. C* **104**, 064609 (2021).
- [41] J. Kelley, E. Kwan, J. Purcell, C. Sheu, and H. Weller, Energy levels of light nuclei  $A=11$ , *Nucl. Phys. A* **880**, 88 (2012).
- [42] M. Cavallaro, J. I. Bellone, S. Calabrese, C. Agodi, S. Burrello, F. Cappuzzello, D. Carbone, M. Colonna, N. Deshmukh, H. Lenske, A. Spatafora, L. Acosta, P. Amador-Valenzuela, T. Borello-Lewin, G. A. Brischetto, D. Calvo, V. Capirossi, E. Chávez, I. Ciraldo, M. Cutuli *et al.*, A constrained analysis of the  $^{40}\text{Ca}(^{18}\text{O}, ^{18}\text{F})^{40}\text{K}$  direct charge exchange reaction mechanism at 275 MeV, *Front. Astron. Space Sci.* **8**, 659815 (2021).
- [43] S. Burrello, S. Calabrese, F. Cappuzzello, D. Carbone, M. Cavallaro, M. Colonna, J. A. Lay, H. Lenske, C. Agodi, J. L. Ferreira, S. Firat, A. Hacisalihoglu, L. La Fauci, A. Spatafora, L. Acosta, J. I. Bellone, T. Borello-Lewin, I. Boztosun, G. A. Brischetto, D. Calvo *et al.*, Multichannel experimental and theoretical constraints for the  $^{116}\text{Cd}(^{20}\text{Ne}, ^{20}\text{F})^{116}\text{In}$  charge exchange reaction at 306 MeV, *Phys. Rev. C* **105**, 024616 (2022).
- [44] S. Nakayama, T. Yamagata, M. Tanaka, M. Inoue, K. Yuasa, T. Itahashi, H. Ogata, N. Koori, and K. Shima, Relative strength  $(\Delta S = 1)/[(\Delta S = 0) + (\Delta S = 1)]$  of isovector spin excitations in the high-lying resonance region of  $^{12}\text{C}$ , *Phys. Rev. Lett.* **67**, 1082 (1991).
- [45] S. Nakayama, T. Yamagata, K. Yuasa, M. Tanaka, H. Bohlen, H. Lenske, H. Wolter, M. Inoue, T. Itahashi, and H. Ogata, Excitation of isovector states by the  $(^7\text{Li}, ^7\text{Be})$  reaction on  $^{12}\text{C}$  and  $^{13}\text{C}$ , *Nucl. Phys. A* **507**, 515 (1990).
- [46] F. Cappuzzello, H. Lenske, A. Cunsolo, D. Beaumel, S. Fortier, A. Foti, A. Lazzaro, C. Nociforo, S. E. A. Orrigo, and J. S. Winfield, Analysis of the  $^{11}\text{B}(^7\text{Li}, ^7\text{Be})^{11}\text{Be}$  reaction at 57 MeV in a microscopic approach, *Nucl. Phys. A* **739**, 30 (2004).
- [47] I. J. Thompson, Coupled reaction channels calculations in nuclear physics, *Comput. Phys. Rep.* **7**, 167 (1988).
- [48] N. Shimizu, T. Mizusaki, Y. Utsuno, and Y. Tsunoda, Thick-restart block Lanczos method for large-scale shell-model calculations, *Comput. Phys. Commun.* **244**, 372 (2019).
- [49] L. C. Chamon, B. V. Carlson, L. R. Gasques, D. Pereira, C. De Conti, M. A. G. Alvarez, M. S. Hussein, M. A. Candido Ribeiro, E. S. Rossi, Jr., and C. P. Silva, Toward a global description of the nucleus-nucleus interaction, *Phys. Rev. C* **66**, 014610 (2002).
- [50] D. Carbone *et al.*, Microscopic cluster model for the description of new experimental results on the  $^{13}\text{C}(^{18}\text{O}, ^{16}\text{O})^{15}\text{C}$  two-neutron transfer at 84 MeV incident energy, *Phys. Rev. C* **95**, 034603 (2017).
- [51] M. Cavallaro, F. Cappuzzello, D. Carbone, A. Cunsolo, A. Foti, and R. Linares, Transport efficiency in large acceptance spectrometers, *Nucl. Instrum. Methods Phys. Res., Sect. A* **637**, 77 (2011).
- [52] B. Paes *et al.*, Long-range versus short-range correlations in the two-neutron transfer reaction  $^{64}\text{Ni}(^{18}\text{O}, ^{16}\text{O})^{66}\text{Ni}$ , *Phys. Rev. C* **96**, 044612 (2017).
- [53] M. Ermamatov, F. Cappuzzello, J. Lubian, M. Cubero, C. Agodi, D. Carbone, M. Cavallaro, J. Ferreira, A. Foti *et al.*, Two-neutron transfer analysis of the  $^{16}\text{O}(^{18}\text{O}, ^{16}\text{O})^{18}\text{O}$  reaction, *Phys. Rev. C* **94**, 024610 (2016).
- [54] M. J. Ermamatov *et al.*, Comprehensive analysis of high-lying states in  $^{18}\text{O}$  populated with  $(t, p)$  and  $(^{18}\text{O}, ^{16}\text{O})$  reactions, *Phys. Rev. C* **96**, 044603 (2017).
- [55] V. A. B. Zagatto, F. Cappuzzello, J. Lubian, M. Cavallaro, R. Linares, D. Carbone, C. Agodi, A. Foti, S. Tudisco, *et al.*, Important role of projectile excitation in  $^{16}\text{O} + ^{60}\text{Ni}$  and  $^{16}\text{O} + ^{27}\text{Al}$  scattering at intermediate energies, *Phys. Rev. C* **97**, 054608 (2018).
- [56] E. N. Cardozo, J. Lubian, R. Linares, F. Cappuzzello, D. Carbone, M. Cavallaro, J. L. Ferreira, A. Gargano, B. Paes, and G. Santagati, Competition between direct and sequential two-neutron transfers in the  $^{18}\text{O} + ^{28}\text{Si}$  collision at 84 MeV, *Phys. Rev. C* **97**, 064611 (2018).
- [57] A. Spatafora, F. Cappuzzello, D. Carbone, M. Cavallaro, J. A. Lay, L. Acosta, C. Agodi, D. Bonanno, D. Bongiovanni, I. Boztosun, G. A. Brischetto, S. Burrello, S. Calabrese, D. Calvo, E. R. Chávez Lomelí, I. Ciraldo, M. Colonna, F. Delaunay, N. Deshmukh, J. L. Ferreira *et al.* (for the NUMEN Collaboration),  $^{20}\text{Ne} + ^{76}\text{Ge}$  elastic and inelastic scattering at 306 MeV, *Phys. Rev. C* **100**, 034620 (2019).
- [58] D. Carbone, J. L. Ferreira, S. Calabrese, F. Cappuzzello, M. Cavallaro, A. Hacisalihoglu, H. Lenske, J. Lubian, R. I. Magaña Vsevolodovna, E. Santopinto, C. Agodi, L. Acosta, D. Bonanno, T. Borello-Lewin, I. Boztosun, G. A. Brischetto, S. Burrello, D. Calvo, E. R. Chávez Lomelí, I. Ciraldo *et al.*, Analysis of two-nucleon transfer reactions in the

- $^{20}\text{Ne} + ^{116}\text{Cd}$  system at 306 MeV, *Phys. Rev. C* **102**, 044606 (2020).
- [59] D. Carbone, R. Linares, P. Amador-Valenzuela, S. Calabrese, F. Cappuzzello, M. Cavallaro, S. Firat, M. Fisichella, A. Spatafora, L. Acosta, C. Agodi, I. Boztosun, G. Brischetto, D. Calvo, E. Chávez Lomelí, I. Ciraldo, M. Cutuli, F. Delaunay, N. Deshmukh, P. Finocchiaro *et al.*, Initial state interaction for the  $^{20}\text{Ne} + ^{130}\text{Te}$  and  $^{18}\text{O} + ^{116}\text{Sn}$  systems at 15.3A MeV from elastic and inelastic scattering measurements, *Universe* **7**, 58 (2021).
- [60] L. La Fauci, A. Spatafora, F. Cappuzzello, C. Agodi, D. Carbone, M. Cavallaro, J. Lubian, L. Acosta, P. Amador-Valenzuela, T. Borello-Lewin, G. A. Brischetto, S. Calabrese, D. Calvo, V. Capirossi, E. R. Chávez Lomelí, I. Ciraldo, M. Cutuli, F. Delaunay, H. Djapo, C. Eke *et al.*,  $^{18}\text{O} + ^{76}\text{Se}$  elastic and inelastic scattering at 275 MeV, *Phys. Rev. C* **104**, 054610 (2021).
- [61] J. L. Ferreira, D. Carbone, M. Cavallaro, N. N. Deshmukh, C. Agodi, G. A. Brischetto, S. Calabrese, F. Cappuzzello, E. N. Cardozo, I. Ciraldo, M. Cutuli, M. Fisichella, A. Foti, L. La Fauci, O. Sgouros, V. Soukeras, A. Spatafora, D. Torresi, and J. Lubian (NUMEN Collaboration), Analysis of two-proton transfer in the  $^{40}\text{Ca}(^{18}\text{O}, ^{20}\text{Ne})^{38}\text{Ar}$  reaction at 270 MeV incident energy, *Phys. Rev. C* **103**, 054604 (2021).
- [62] I. Ciraldo, F. Cappuzzello, M. Cavallaro, D. Carbone, S. Burrello, A. Spatafora, A. Gargano, G. De Gregorio, R. I. Magaña Vsevolodovna, L. Acosta, C. Agodi, P. Amador-Valenzuela, T. Borello-Lewin, G. A. Brischetto, S. Calabrese, D. Calvo, V. Capirossi, E. R. C. Lomelí, M. Colonna, F. Delaunay *et al.* (For the NUMEN Collaboration), Analysis of the one-neutron transfer reaction in  $^{18}\text{O} + ^{76}\text{Se}$  collisions at 275 MeV, *Phys. Rev. C* **105**, 044607 (2022).
- [63] J. L. Ferreira, J. Lubian, F. Cappuzzello, M. Cavallaro, and D. Carbone (NUMEN Collaboration), Multinucleon transfer in the  $^{116}\text{Cd}(^{20}\text{Ne}, ^{20}\text{O})^{116}\text{Sn}$  double charge exchange reaction at 306 MeV incident energy, *Phys. Rev. C* **105**, 014630 (2022).
- [64] M.A.G. Alvarez, L. Chamon, M. Hussein, D. Pereira, L. Gasques, E. Rossi, Jr., and C. Silva, A parameter-free optical potential for the heavy-ion elastic scattering process, *Nucl. Phys. A* **723**, 93 (2003).
- [65] D. Pereira, J. Lubian, J. R. B. Oliveira, D. P. de Sousa, and L. C. Chamon, An imaginary potential with universal normalization for dissipative processes in heavy-ion reactions, *Phys. Lett. B* **670**, 330 (2009).
- [66] G. Satchler and W. Love, Folding model potentials from realistic interactions for heavy-ion scattering, *Phys. Rep.* **55**, 183 (1979).
- [67] M. Brandan and G. Satchler, The interaction between light heavy-ions and what it tells us, *Phys. Rep.* **285**, 143 (1997).
- [68] E. Crema, D. R. Otomar, R. F. Simões, A. Barioni, D. S. Monteiro, L. K. Ono, J. M. B. Shorto, J. Lubian, and P. R. S. Gomes, Near-barrier quasielastic scattering as a sensitive tool to derive nuclear matter diffuseness, *Phys. Rev. C* **84**, 024601 (2011).
- [69] E. Crema, V. A. B. Zagatto, J. M. B. Shorto, B. Paes, J. Lubian, R. F. Simões, D. S. Monteiro, J. F. P. Huiza, N. Added *et al.*, Reaction mechanisms of the  $^{18}\text{O} + ^{63}\text{Cu}$  system at near-barrier energies, *Phys. Rev. C* **98**, 044614 (2018).
- [70] L. M. Fonseca, R. Linares, V. A. B. Zagatto, F. Cappuzzello, D. Carbone, M. Cavallaro, C. Agodi, J. Lubian, and J. R. B. Oliveira, Elastic and inelastic scattering of  $^{16}\text{O}$  on  $^{27}\text{Al}$  and  $^{28}\text{Si}$  at 240 MeV, *Phys. Rev. C* **100**, 014604 (2019).
- [71] B. Pritychenko, M. Birch, B. Singh, and M. Horoi, Tables of E2 transition probabilities from the first  $2^+$  states in even-even nuclei, *At. Data Nucl. Data Tables* **107**, 1 (2016).
- [72] T. Kibedi and R. H. Spear, Reduced electric-octupole transition probabilities,  $B(E3; 0_1^+ \rightarrow 3_1^-)$ —An update, *At. Data Nucl. Data Tables* **80**, 35 (2002).
- [73] Y. Utsuno and S. Chiba, Multiparticle-multihole states around  $^{16}\text{O}$  and correlation-energy effect on the shell gap, *Phys. Rev. C* **83**, 021301(R) (2011).
- [74] E. K. Warburton and B. A. Brown, Effective interactions for the  $0p1s0d$  nuclear shell-model space, *Phys. Rev. C* **46**, 923 (1992).